Mapping the Path to Cryogenic Atom Probe Tomography Analysis of Biomolecules

Eric V Woods, Tim M Schwarz, Mahander P Singh, Shuo Zhang, Se-Ho Kim, Ayman A El-Zoka, Lothar Gremer, Dieter Willbold, Ingrid McCarroll, Baptiste Gault

DECTRIS

ARINA with NOVENA

Fast 4D STEM

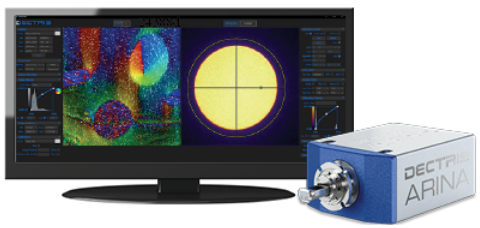

DECTRIS NOVENA and CoM analysis of a magnetic sample.

Sample courtesy: Dr. Christian Liebscher, Max-Planck-Institut für Eisenforschung GmbH.
Experiment courtesy: Dr. Mingjian Wu and Dr. Philipp Pelz, Friedrich-Alexander-Universität, Erlangen-Nürnberg.

Downloaded from https://academic.oup.com/mam/article/31/4/ozaf032/8211905 by Forschungszentrum Juelich GmbH Zentralbibliothek user on 27 August 2025

Microscopy and Microanalysis, 2025, **31**, ozaf032
https://doi.org/10.1093/mam/ozaf032
Advance access publication 24 July 2025
Original Article

Microscopy AND Microanalysis

Mapping the Path to Cryogenic Atom Probe Tomography Analysis of Biomolecules

Eric V. Woods[1,*], Tim M. Schwarz[1], Mahander P. Singh[1], Shuo Zhang[1], Se-Ho Kim[1,2], Ayman A. El-Zoka[1,3], Lothar Gremer[4,5], Dieter Willbold[4,5], Ingrid McCarroll[1], and Baptiste Gault[1,3,*]

[1]*Microstructure Physics and Alloy Design, Max Planck Institute for Sustainable Materials (formerly known as Max-Planck-Institut für Eisenforschung GmbH), Max-Planck-Str. 1, Düsseldorf 40237, Germany*
[2]*Department of Materials Science and Engineering, Korea University, 145 Anam-ro, Seongbuk District, Seoul 02841, Republic of Korea*
[3]*Department of Materials, Royal School of Mines, Imperial College London, Prince Consort Rd, South Kensington, London SW7, UK*
[4]*Department Biologie, Institut für Physikalische Biologie, Heinrich-Heine-Universität Düsseldorf, Universittstraße 1, Düsseldorf 40225, Germany*
[5]*Structural Biochemistry (IBI-7), Institute of Biological Information Processing, Forschungszentrum Jülich, Wilhelm-Johnen-Straße 1, Jülich 52425, Germany*

***Corresponding authors:** Eric V. Woods, E-mail: e.woods@mpie.de; Baptiste Gault, E-mail: b.gault@mpie.de

Abstract

The understanding of protein structure and interactions remains a fundamental challenge in modern biology. While X-ray and electron-based techniques have provided atomic-level protein configurations, they require numerous molecules for averaged views and lack detailed compositional information crucial for biochemical activity. Atom probe tomography (APT) emerges as a promising tool for biological material analysis, though its capabilities for examining biomolecules in their native, hydrated state remain largely unexplored. We present systematic analyses of amino acids in frozen aqueous solutions using two different nanoporous metal supports across various analysis conditions. Our methodology employs a complete cryogenic workflow, including drop-casting, inert gas glovebox freezing, and specimen transfer via a cryogenically cooled ultra-high vacuum shuttle to both focused ion beam microscopy and atom probes. Using water molecular ion ratios as electrostatic field condition indicators, we investigate amino acid fragmentation and behavior. We evaluate the critical factors for successful biomolecular analysis: support material selection, cryogenic specimen preparation, and optimal data acquisition parameters. This work establishes guidelines for cryogenic APT analysis of biomolecules, advancing the technique's application in biological sciences.

Key words: APT, cryogenic, spectroscopy, tomography, water

Introduction

Since proteins and biomolecules are fundamental to life, the analysis of their interactions and configuration is crucial for understanding biological functionality. Primary protein structure consists of an initially linear chain of 20 canonical amino acids, which share a common backbone in their free state. This backbone contains a carboxyl group and an amine group, which are subsequently chemically joined to form a peptide bond during synthesis (Kessel & Ben-Tal, 2018). The variable portion is a side group, which consists of a wide variety of different chemical configurations, chain lengths, and positive and negative charges, e.g., exposed hydroxyl and amine groups, which can serve as bonding sites for enzymes to later perform post-translational modification binding (Bobalova et al., 2023; Lee et al., 2023). Some additional information regarding protein structure can be found in the Supplementary Material, in the "Note on Protein Structure" section. As the protein emerges from the ribosome during synthesis, the side groups of the protein drive folding into certain common motifs, such as α-helices and β-sheets, which comprise the secondary structure (Kessel & Ben-Tal, 2018). Other cellular machinery, such as chaperone proteins, may assist the nascent protein to achieve its stable larger, three-dimensional (3D) ternary form (Balchin et al., 2020). Finally, the folded protein may be assembled into larger macromolecular complexes, so-called quaternary structures, including respiratory complexes, nuclear pores, etc. (Marsh & Teichmann, 2015).

As a part of this process, the protein may be complexed with metal ions, such as iron and magnesium, to catalyze functions such as oxygen transport, chemical transformation, and a whole panoply of other reactions essential to life that require co-factors to perform (Ajioka et al., 2006). Characterizing the interaction of metal ions with proteins, for example, is an exceptionally challenging process in the dynamic, ever-changing environment of a cell. These fleeting interactions are critical to life processes, and are known to generate reactive oxygen species, and both copper and iron are implicated in Alzheimer's disease and many other neurological disorders (Chen et al., 2023). Studying the structure of native proteins has been revolutionized by the availability of cryogenic transmission electron microscopy (cryo-TEM) (Dubochet et al., 1988; Sigworth, 2016; Halfon et al., 2022), but it has significant challenges in elemental identification for metal ion interactions, with cryo-scanning TEM (cryo-STEM) partially overcoming this to a limited extent (Elad et al., 2017; Herdman et al., 2022). For studying proteins' chemistry in their native state, tandem mass spectrometry (MS) is the other state-of-the-art technique (Shuken, 2023). The two techniques

Received: December 4, 2024. **Revised:** March 27, 2025. **Accepted:** April 15, 2025
© The Author(s) 2025. Published by Oxford University Press on behalf of the Microscopy Society of America.
This is an Open Access article distributed under the terms of the Creative Commons Attribution License (https://creativecommons.org/licenses/by/4.0/), which permits unrestricted reuse, distribution, and reproduction in any medium, provided the original work is properly cited.

Downloaded from https://academic.oup.com/mam/article/31/4/ozaf032/8211905 by Forschungszentrum Juelich GmbH Zentralbibliothek user on 27 August 2025

provide complementary information but on scales that are difficult to reconcile, failing to provide full 3D elemental identification and positional information at a sub-nanometre scale.

Atom probe tomography (APT) can achieve elemental and ionic mapping in 3D with sub-nanometre spatial resolution (Devaraj et al., 2017; Gault et al., 2021). APT's potential to address many open, outstanding biological questions has been discussed for decades (Panitz, 1982, 2005; Kelly et al., 2009), but studies beyond proof-of-principle are rare and focused primarily on hard biominerals (Gordon & Joester, 2011; La Fontaine et al., 2016; Grandfield et al., 2022).

During APT analysis, a sharp needle-shaped specimen is maintained at cryogenic temperatures and subjected to a high DC electrostatic field on which are superimposed either voltage pulses (Müller et al., 1968), laser pulses (Gault et al., 2006; Bunton et al., 2007), or a combination of both (Zhao et al., 2017; Taniguchi & Nishikawa, 2019). The pulses drive the field evaporation of individual atomic or molecular ions, which are collected by a position-sensitive, time-resolved detector, recording simultaneously a two-dimensional (2D) ion impact position, and a time-of-flight converted into a mass-to-charge ratio (Blavette et al., 1993; Larson et al., 2013). This data is processed to produce a 3D point cloud reconstituting the distribution of species in the original specimen (Vurpillot et al., 2013).

APT specimens are needle shaped, sharpened to an apex tip radius less than 100 nm in diameter, and are usually prepared using a dual-beam scanning electron microscope/focused ion beam (SEM/FIB) system (Prosa & Larson, 2017). Typically, a bulk sample is loaded onto the stage, tilted perpendicular to either a Ga or Xe plasma ion beam, and a 2–3 μm thick lamella is prepared. The stage is tilted back to a horizontal position, and it is attached to an inserted tungsten micromanipulator using metal deposited from an organometallic precursor and cut free of the bulk. The lamella is cut into small 2 μm sections, sequentially placed onto an array of silicon microtips on a silicon coupon via attachment with metal and cutting each section with the ion beam. Subsequently, the silicon microtips are tilted normally to the ion beam and sharpened using annular milling, where both the ion beam current and the inner diameter of the circle are decreased until an apex radius of less than 100 nm is achieved. In this way, many APT specimens can be rapidly and efficiently prepared at one time from specific sites on a bulk sample. Alternatively, a liquid sample of amyloid-beta protein fibrils can be dipped into a liquid and dried before placing into an atom probe, although the resultant mass spectrum only contained low-mass hydrocarbons (Rusitzka et al., 2018). As a comparison, frozen amyloid-beta liquid samples easily yield atomic-scale structural information using cryo-TEM (Gremer et al., 2017; Becker et al., 2023).

For wet or hydrated samples, historically sample preparation has been extremely challenging. The liquid must be placed onto some kind of support material, and then subsequently frozen; depending on the application, vitrification may be used to avoid ice crystal formation and sample damage. Subsequently, the specimen must be maintained at cryogenic temperatures to prevent ice crystal formation, particularly within a vitrified sample. Ideally, to avoid frost buildup, handling of frozen samples must be carried out in inert gas gloveboxes either before or after the liquid sample is frozen, and it can never be exposed to gas containing moisture or it will almost instantly suffer from frosting. Since FIBs are typically used to make the samples, ultra-high vacuum (UHV) transfer shuttles facilitate sample transfer between instruments. Several groups have developed integrated cryogenic instrumental suites and workflows (Gerstl & Wepf, 2015; Perea et al., 2017; Stephenson et al., 2018) or built coupled FIB/SEM atom probe systems (Stender, 2022*a*, 2022*b*). The FIB needs to have a cryogenic sample and be loaded under a vacuum, for the reasons previously described. Specimen preparation has been reported from the edge of frozen droplets on nanoporous flat substrates (El-Zoka et al., 2020), nanoporous metal needles (Tegg et al., 2024), or from very large droplets placed on wire-shaped substrates (Schwarz et al., 2020, 2021). Site-specific liftout of a 2–3 μm thick lamella at cryogenic temperature, subsequently mounted on APT multi-needle specimen carrier without the use of metal-based deposition using a gas injection system was also demonstrated (Perea et al., 2008; Schreiber et al., 2018; Klumpe et al., 2022), and further refined to enable more routine cryogenic specimen preparation (Douglas et al., 2023), including liftout of frozen liquid water without any support material (Woods et al., 2023*b*).

Biologically interesting molecules occur in living systems, which are water-based. Furthermore, the proteins exist in a cellular environment where they are surrounded by water, other proteins and binding partners, and many light element ions. Without water, such proteins misfold and aggregate, and their functionality is destroyed. Their associations with light elements or metal ions can also cause modification and deactivation. Furthermore, proteins are inherently ionized, i.e., the different constituent amino acids carry charges, which control their structure and function. In order to analyze organic molecules using APT, particularly proteins in their native state in association with metal ions, binding partners, etc., they must be in their ionized state. This explains why this work has focused here on studying the fragmentation of model systems, in this case single amino acids, and field evaporation of the aqueous matrix. Individual amino acids and proteins, e.g., amyloid fibrils in solution, prepared via drop-casting, performed by placing a drop of liquid and allowing the liquid to evaporate, did not yield structural information but rather tiny fragments (Rusitzka et al., 2018). Conversely, individual amino acids, prepared via drop-casting an amino acid solution onto a carbon nanotube (CNT) mesh and dried, were previously studied using APT (Nishikawa et al., 2011; Taniguchi & Nishikawa, 2016; Nishikawa & Taniguchi, 2017). Larger mass fragments were recovered in that case, but without the matrix material, i.e., the liquid, the applicability to understanding the native structure of hydrated proteins and their constituent amino acids is likely limited, both because the electrostatic field conditions are likely significantly different and the amino acids exist in ionized form, i.e., the carboxyl and amino groups are in zwitterionic form any side chains are also charged. Significant work has gone into understanding the field emission behavior of water in conjunction with theoretical work (Anway, 1969; Stintz & Panitz, 1991, 1992; Pinkerton et al., 1999; Stuve, 2012). In APT specifically, pure water has been analyzed in free-standing specimens (El-Zoka et al., 2020; Schwarz et al., 2020; Segreto et al., 2022), graphene-encapsulated needles (Qiu et al., 2020*a*, 2020*b*), and on or in nanoporous metal substrates (Tegg et al., 2021, 2024; Stender, 2022*a*, 2022*b*; Woods et al., 2023*a*).

Building on previous work, our group has previously established a full cryogenic transfer chain, to freeze a liquid sample in an inert gas glovebox and routinely prepare APT specimens

Downloaded from https://academic.oup.com/mam/article/31/4/ozaf032/8211905 by Forschungszentrum Juelich GmbH Zentralbibliothek user on 27 August 2025

from that material. There is a clear need to advance the state-of-the-art in the analysis of water-based organic solution APT data. Here, we present the results of an effort to characterize single amino acids in a water matrix on nanoporous metals, as model systems to understand their fragmentation patterns. Data are presented for cysteine, lysine, and arginine, on two substrates, nanoporous gold (NPG) and nanoporous copper (nanoporous Cu) from a CuZn alloy. Selected samples are analyzed with two different local electrode atom probes (LEAP) and across a wide range of analysis conditions. These datasets allow us to outline guidelines for the analysis of amino acids and more complex biomacromolecules that will help establish best practices for this burgeoning field.

Results

Water Matrix

Field evaporation of organic, and generally nonmetallic, materials leads to the formation of molecular or cluster ions that can dissociate into smaller fragments. The fragmentation path depends on the electrostatic field conditions. This requires identifying a reliable descriptor to estimate the electrostatic field strength across different water-containing datasets, to facilitate systematic analyses to understand, and possibly predict, the results of the fragmentation process. For metallic systems, or semiconductors, the ratio of the charge states of an element is often used as a proxy for the local electrostatic field (Kingham, 1982; Schreiber et al., 2014; Gault et al., 2016; Cuduvally et al., 2022). For metallic materials in APT, a charge state ratio (CSR) of two different ionization states is typically defined to compare datasets. As an example, for W where W^{3+} is the dominant species, a typical CSR would be W^{3+}/W^{2+}. There are no standard definitions for CSR in the APT community; in the literature, lower abundance ions could be in the denominator or numerator. Additionally, reported experimental values can vary over a wide range; for presharpened silicon microtips, measured values for Si^{2+}/Si^{+} can be between 0.01 and 100. In this work, since water is the typical matrix for biomolecules, defining a descriptor associated with the mass spectra obtained from the analysis of water appears to be the most reasonable choice (Exertier et al., 2024; Tegg et al. 2024).

Preliminary work demonstrated that water field evaporated in the form of protonated water cluster ions with a formula $(H_2O)_nH^+$ (Stintz & Panitz, 1992; El-Zoka et al., 2020; Schwarz et al., 2020), and their relative abundance is an indicator of the electrostatic field strength. Here, we considered 20 individual datasets, summarized in Table 1, some containing data acquired across a range of laser pulse energies, and the three most abundant ions were for $n = 1, 2, 3$, overall in that order of abundance, with mass-to-charge of 19, 37, and 55 Da, respectively (Schwarz et al., 2020). At higher field strengths, the signal for higher-order water clusters above $n = 3$ is below the level of background.

We can hence define an analogous cluster ion ratio (CIR) as $\sum_{n=1}^{n=3}(H_2O)_nH^+/(H_2O)_3H^+$. Our definition of the CIR is justified for two reasons. First, we based our choice on the published literature. Stintz & Panitz (1993) reported that the relative amplitude of the water cluster ions varied as a function

Table 1. APT data acquisition conditions, data size, and specimen/substrate type.

Run	Straight (XS) or Reflectron (XR)	Ion Count (Total)	Laser / Voltage	Laser Power (pJ)	Pulse Rate (kHz)	Temperature (K)	Detection Rate (%)	Pulse Fraction (%)	Analyte Solution	Substrate
1	XS	27 M	Laser	60	125	60	0.5		Fibrils in water	AuAg
2	XS	7.9 M	Laser	40	Varied	50	1		Cysteine in water 0.1 M	AuAg
3	XS	13.8 M	Voltage		100	50	0.3	15	Cysteine in water 0.1 M	AuAg
4	XS	27.2 M	Laser	Varied	200	50	0.5		Cysteine in water 0.1 M	AuAg
5	XS	15 M	Laser	60	125	50	0.5		Cysteine 0.1 M in D_2O	AuAg
6	XS	4.3 M	Laser	40	Varied	50	Varied		Cysteine in water 0.1 M	AuAg
7	XS	15 M	Laser	Varied	200	50	0.5		Lyine 0.1 M in water	AuAg
8	XS	13 M	Laser	40	200	50	0.5		Lyine 0.1 M in water	AuAg
9	XS	5 M	Laser	40	200	50	0.5		Arginine 0.1 M	AuAg
10	XS	31 M	Laser	50	200	50	0.5		Arginine 0.1 M	CuZn
11	XS	124 M	Laser	Varied	200	50	0.8		Arginine 0.1 M in water	CuZn
12	XS	5 M	Laser	80	125	60	0.5		Cysteine 0.1 M in water	CuZn
13	XS	59 M	Laser	Varied	Varied	60	0.5		Lysine 0.1 M in water	Cu
14	XR	2 M	Laser	55	Varied	50	Varied		Cysteine 0.1 M in water	CuZn
15	XR	1 M	Laser	55	125	50	0.8		Cysteine 0.1 M in water	CuZn
16	XS	24 M	Laser	80	125	60	0.5		Cysteine 0.1 M in water	CuZn
17	XS	0.5 M	Laser	60	125	50	0.6		Cysteine 0.1 M in water	CuZn
18	XS	25 M	Laser	35	100	60	0.6		Lysine 0.1 M in water	CuZn
19	XS	3 M	Laser	58	100	60	0.7		Lysine 0.1 M in water	CuZn
20	XR	4.3 M	Laser	76	125	50	0.5		Water	AuAg
21	XR	5 M	Laser	76	125	50	0.5		Water	AuAg
22	XR	4 M	Laser	67	125	50	0.5		Water	AuAg
23	XR	6 M	Laser	Varied	100	50	1		Water	GaIn
24	XR	26 M	Laser	78	125	50	0.5		Water	Cu
25	XR	27 M	Laser	61	125	60	0.5		Water	Cu/Cr
26	XR	2 M	Laser	80	100	50	0.45		Water	Cu
27	XR	2 M	Laser	Varied	Varied	50	Varied		Water	AuAg
28	XR	4.4 M	Laser	67	125	50	0.8		Water	AuAg
29	XR	1.2 M	Voltage		Varied	50	0.75	15	Water	AuAg
30	XR	1.8 M	Laser	85	125	50	1		Water	AuAg

Downloaded from https://academic.oup.com/mam/article/31/4/ozaf032/8211905 by Forschungszentrum Juelich GmbH Zentralbibliothek user on 27 August 2025

of the field evaporation temperature and hence electrostatic field, which is what we sought to address with the CIR. Second, over the analyses of the many datasets, we have collected in recent years, both those containing only water, and water with bio(macro)molecules, only water clusters ranging up to $n = 3$, i.e., $(H_2O)_3H^+$ are always guaranteed to be present, regardless of the dataset size. Therefore, the sum of $n = 1, \ldots, 3$ water clusters was logically selected as numerator, in order for the ratio to be greater than 1 for practical reasons. Since the $n = 3$ peak is the one that showed the greatest range of variations across datasets, which again agrees with previous reports, it seemed logical for it to be selected for the CIR. This CIR can be considered a suitable descriptor for the electrostatic field conditions, which will be used hereafter.

Practically, this means that datasets with a relatively higher CIR have a local electrostatic field which is substantially higher than that of a dataset with a lower CIR. A low CIR will have more water clusters, $(H_2O)_nH^+$, where n is the cluster order, probably at least $n = 1, \ldots, 8$. Previous work has illustrated that water clusters up to $n = 18$ are possible (Woods et al., 2023*a*, 2023b, 2024). A dataset with high CIR would be expected to suppress larger protonated water clusters, such that only a few clusters over $n = 3$ are visible over the background. With a lower CIR, the local electrostatic field is lower, and therefore, larger clusters are energetically favorable (Stuve, 2012).

The reason for the disappearance of higher-order water peaks, as shown in data later, results from both the peak abundance decreasing with increasing CIR and a rise in the background, with the local electrostatic field, i.e., that peak abundance changes with increasing CIR and background can also rise. In addition, in most datasets, the difference in abundance of the $n = 1$ and $n = 2$ varied within a similar, limited range. These observations agree with the previously mentioned references. The intensity of other fragment ions, e.g., OH^+ or H_2O^+, did not reliably or consistently provide more information or match the electrostatic field or laser power. Water clusters $n = 2$ and higher did not show side, smaller peaks above the background.

Figure 1 plots logarithmically the relative abundance of the protonated water clusters, specifically on the x-axis the sum of water clusters $\sum(H_2O)_{n=1,2,3}H^+$ is divided by $(H_2O)_3H^+$, and the y-axis is $(H_2O)_1H^+$ divided by $\sum(H_2O)_{n=1,2,3}H^+$, across the 20 datasets, split into subsets containing 1 million ions. The symbol represents the biomolecule in the solution, the interior fill color represents the laser pulse energy (LPE), and black represents data acquired in high-voltage pulsing mode. The symbol with a black border was obtained using NPG as a substrate, which was taken on a straight flight path (XS) instrument, whereas the red and green border are data acquired with a nanoporous Cu substrate, respectively, on a straight flight path (XS) or reflectron-fitted (XR) instrument. There was no notable difference between data taken on the XS and XR instruments, or between data from NPG or nanoporous copper substrates. Run conditions for the different runs are noted in Table 1, which can be found in the Supplementary Material. All solutions were prepared in Type 1 deionized (DI) water unless otherwise noted. Some runs had variable parameters, so "varied" is written in the field(s) which was changed. Other runs had certain parts of the total run excluded (specimen started running, microfracture, etc.), so the ion total listed in the table may not match the extracted region used in a particular figure. Theoretically, increasing LPE should increase the specimen temperature, resulting in a decrease in the local electrostatic field; in practice, we showcase here, particularly through Figure 1, that this is much complex, with numerous other parameters influencing the results, including the specimen length, its geometry, and shape evolution, along with local segregated regions of higher organic concentrations created by slow freezing in some cases.

This graph is admittedly complex but showcases general trends. Overall, the field conditions do not directly correlate with the instrument used or the LPE. This is expected because the thermal pulse arising from the laser absorbed by the specimen depends on numerous factors (Vurpillot et al., 2009; Houard et al., 2011; Kelly et al., 2014), including, for example, the specimen's geometry, i.e., radius and shank angle (Bunton et al., 2007). These even vary over the course of a single analysis, including through a loss of cylindrical symmetry from the side first illuminated by the laser (Sha et al., 2008), along with material or structural inhomogeneities. The refractive index and UV absorption coefficients of the substrates, considered as bulk Au and Cu, respectively, are

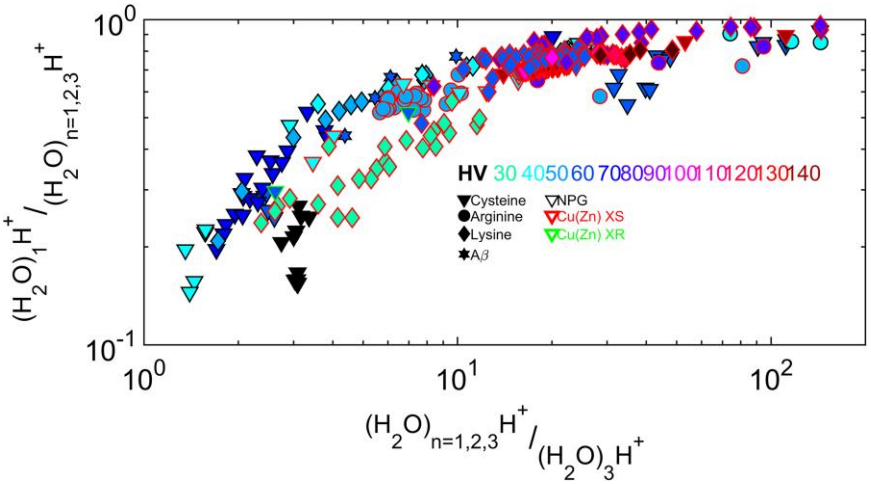

Fig. 1. Plot of $n = 1$, $(H_2O)_1H^+$, normalized by the sum of water clusters $n = 1, 2, 3$, $(H_2O)_nH^+$, as a function of the $n = 3$, $(H_2O)_3H^+$, similarly normalized. The colored numbers represent the LPE, specified in picojoules (pJ), used in the interior color of each symbol.

Downloaded from https://academic.oup.com/mam/article/31/4/ozaf032/8211905 by Forschungszentrum Juelich GmbH Zentralbibliothek user on 27 August 2025

similar enough to neglect, e.g., refractive indices n of 1.5 and 1.37 and absorption factor k of 1.886 and 1.916 at 355 nm/3.5 eV, respectively, and thus absorption coefficients (Johnson & Christy, 1972). The UV laser absorption coefficient for water in an external electrostatic field, along with any material in solution was not considered here, but in general is quite low compared with metallic substrates, oxides, etc. (Warren, 1984) and can be effectively regarded as minimal, similar to many oxides (Silaeva et al., 2014). The UV absorption coefficients for every solution would have to be individually determined under the conditions of intense electrostatic field and are not known to the authors.

The specimen's length is known to influence the amplitude of the electrostatic field (Silaeva et al., 2013, 2014). Here, the length was not recorded systematically and it was variable from specimen to specimen in the range of 3–9 μm approximately. This surely underpins some of the variations observed in the results in Figure 1, as suggested by the literature. The tip lengths were not standardized, which is a limitation of this work. The data obtained in HV pulsing could have been expected to lead to the highest electrostatic field conditions, yet recent reports indicate a more complex behavior for the field evaporation of water under intense field conditions (Schwarz et al., 2020; Segreto et al., 2022). Some data (cysteine on Cu(Zn) in the XS, red triangles) clearly diverge from the main trend, which may be due to longer specimens (Anway, 1969; Woods et al., 2023*b*) or, as will be discussed below, a large amount of metallic impurities.

Generally, though, the data aligns on a positive slope, which matches the expected behavior from previous reports (Pinkerton et al., 1999; Stuve, 2012; Ghesquière et al., 2015; Segreto et al., 2022). This is encouraging as it shows that the relative fraction of $(H_2O)_3H^+$ can inform on the electrostatic field conditions.

Lysine

We first focus on lysine, with a chemical formula $C_6H_{13}N_2O_2$ and a mass of 146 Da. In Figure 2a, a mass spectrum obtained from an APT measurement of lysine HCl in DI water is plotted, along with the chemical structure inset in the upper right. The substrate was NPG, but the final apex of the APT specimen was located far from the metal substrate (3–5 μm). Salient features include (i) protonated water cluster ions, $(H_2O)_nH^+$, where $n = 1, \ldots, 9$, labeled in blue, with their respective locations indicated by the blue semi-transparent vertical bars and (ii) organic fragments originating from lysine, which are not detected compared with the analysis of pure DI water, are labeled in red. Post-evaporation ionization can and does occur, and therefore multiply charged ions/molecules (Ghesquiere et al., 2015; Zanuttini et al., 2017; Peng et al., 2019; Di Russo et al., 2020) can be detected, which further complicates the unambiguous identification of the signals. Secondly, larger molecules can dissociate during their flight to the detector, and identifying their parent molecular ions is important for possible spatial reconstruction. This can be achieved using correlated ion evaporation histograms (Saxey, 2011) generated by multiple hits on the detector created during a single pulse. In such a correlated evaporation histogram, ion tracks that show horizontal and vertical lines correspond to the field evaporation triggered by the laser or high-voltage pulse. Lines that appear parallel to the line of equality of the plot with positive slope, which in reality follow a square root trend, demonstrate delayed evaporation, i.e., the field evaporation of an ion after the field evaporation of an ion was already triggered by the laser/voltage pulse. Such lines demonstrate that those ions underwent no post-evaporation ionization or field-induced dissociation or fragmentation of molecular or cluster ions during the flight toward the detector, which would appear as a curved line with a negative slope (Saxey, 2011). A correlated evaporation histogram for the lysine in water analysis, shown in Supplementary Figure S1, shows no indication of post-evaporation dissociation.

The fragments were identified based on likely breakdown pathways from literature including different electrospray MS techniques (Friedman, 1977; Zhang et al., 1999, 2019; Forbes et al., 2007), along with APT analyses of single amino acid and dipeptide data in dried form (Nishikawa et al., 2011; Taniguchi et al., 2012; Taniguchi & Nishikawa, 2016; Nishikawa & Taniguchi, 2017); single protein APT data (Qiu et al., 2020*b*); and APT data of organic-rich portions of collagen in bone, which consist of proline or hydroxyproline, glycine, and some other amino acids (Langelier et al., 2017; Lee et al., 2021; Grandfield et al., 2022; Holmes et al., 2023) and the assumption to have only single-charged molecules. However, an unambiguous identification of the signals is difficult due to an overlap of certain protonated water cluster ions with organic fragments, for instance, the protonated water cluster with $n = 8$, $(H_2O)_8H^+$, has mass-to-charge 145 Da, which precludes measurement of unprotonated lysine (mass-to-charge 145 Da) or protonated lysine (mass-to-charge 146 Da) that may have appeared. Additionally, certain masses are simply hard to unambiguously assign: drop-cast and dried lysine had a characteristic APT fragment signal, assigned as $CONH^+$ at 43 Da, with additional smaller peaks at 42 and 44 Da (likely de-protonated and protonated forms, respectively) (Taniguchi & Nishikawa, 2016; Nishikawa & Taniguchi, 2017). In the current work with aqueous solutions, the 44 Da peak is assigned as CO_2^+, but there can be a contribution from $CONH_2^+$ and possibly $C_3H_8^+$, although those ions would be indistinguishable based on their mass-to-charge alone, presuming singly charged ions and molecules. Across the references discussed previously, primarily the mass-to-charge 44 Da was assigned to CO_2^+ or $CONH_2^+$, where $C_3H_8^+$ was found in dried organics (Nishikawa et al., 2011; Rusitzka et al., 2018).

As shown in Figure 2b, incomplete dealloying or cleaning of the NPG substrate can result in both Au and Ag dissolving into the solution. Au is labeled in yellow, and Ag is labeled in gray. The correlated evaporation histogram in Supplementary Figure S2 shows no indication of post-evaporation dissociation. Water cluster ions with $n = 1$–5 are observed, but any higher mass ones would be occluded by the metal peaks. Enlarged views of the mass spectral ranges where specific Ag and Au metal–water or metal–organic complexes form in the mass spectrum are displayed for Ag in Supplementary Figure S3 and for Au in Supplementary Figure S4, respectively. These Au–O and Ag–O peaks are consistent with previous APT results for water-filled dealloyed NPG (El-Zoka et al., 2020). These demonstrate that both Ag and Au form molecular and/or cluster ions complexed with CO^+ and/or CO_2^+ ions in aqueous matrices. While noting that the –CO group could also be $–CNH_2$, these ions were previously unreported in aqueous matrices. The lysine fragments seem to be binding to the metallic ions in the solution, which could modify a particular amino acid's mass spectra and fragmentation, possibly complicating future attempts at quantification

Downloaded from https://academic.oup.com/mam/article/31/4/ozaf032/8211905 by Forschungszentrum Juelich GmbH Zentralbibliothek user on 27 August 2025

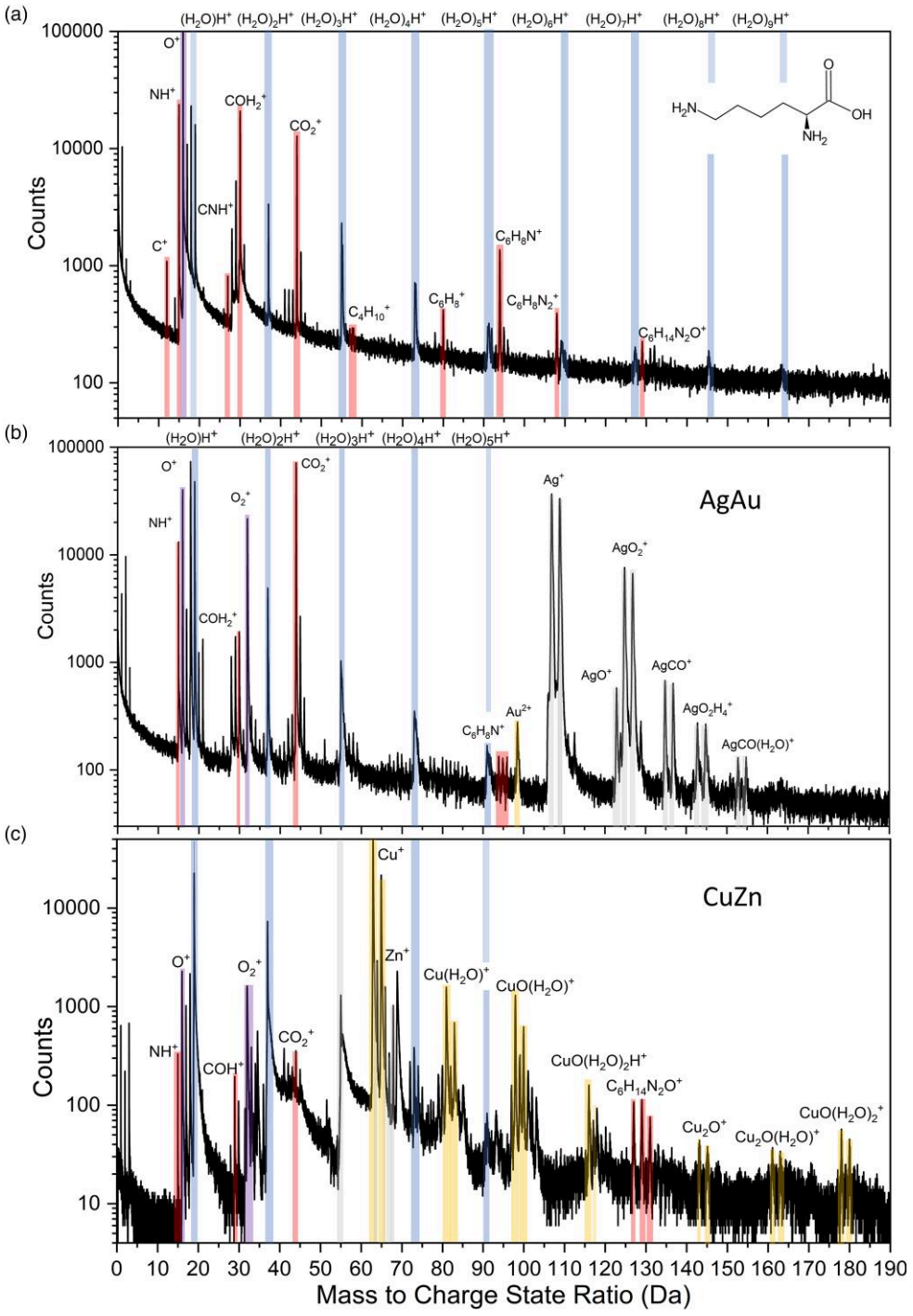

Fig. 2. Mass spectra for lysine 0.1 M in Type 1 water solution (**a**) in Type 1 ultrapure DI water on NPG, with no apparent metal (12.4 million ions, CIR: 4.14, XS, Run 8, Bin: 0.1 Da), with the chemical structure of lysine inset in the upper right (**b**) with Ag and Au ions from NPG substrate (6 million ions, CIR: 10.2, XS, Run 9, Bin: 0.1 Da), substrate name inset on right (**c**) with Cu and Zn ions from CuZn metal substrate (3 million ions, CIR: 9.76, XS, Run 20, Bin: 0.1 Da), substrate name inset on right. The colored lines serve as visual emphasis for particular labeled ions, in all figures, red is organics, blue is $(H_2O)_nH^+$, and purple is ions which are possibly inorganic fragments. In (**b**), gray is Ag, but in (**c**), gray is Zn. Darker yellow is Au in (**b**) and Cu in (**c**).

using APT. In this case, the metal ions are overwhelm any purely organic signal from the analyte, making identification and imaging of, for example, protein backbones extremely challenging. Practically, it means that when analyzing ion locations (and visualizing, for example, protein backbones) on nanoporous metal substrates, mass peaks for specific metal–CO^+ and metal–CO_2^+ ions must be included in the analysis.

Figure 2c illustrates the same phenomena for Cu and Zn, although Zn is almost completely removed from the substrate (Woods et al., 2023*a*); Cu peaks are labeled in yellow, and Zn is labeled in gray. The Cu peaks dominate the mass spectra, shown in more detail in Supplementary Figure S5, and make it extremely difficult to see any organic fragments from lysine. There are mass peaks associated with hydrated Cu oxides which are labeled. In this mass spectrum, none of their individual peak

Downloaded from https://academic.oup.com/mam/article/31/4/ozaf032/8211905 by Forschungszentrum Juelich GmbH Zentralbibliothek user on 27 August 2025

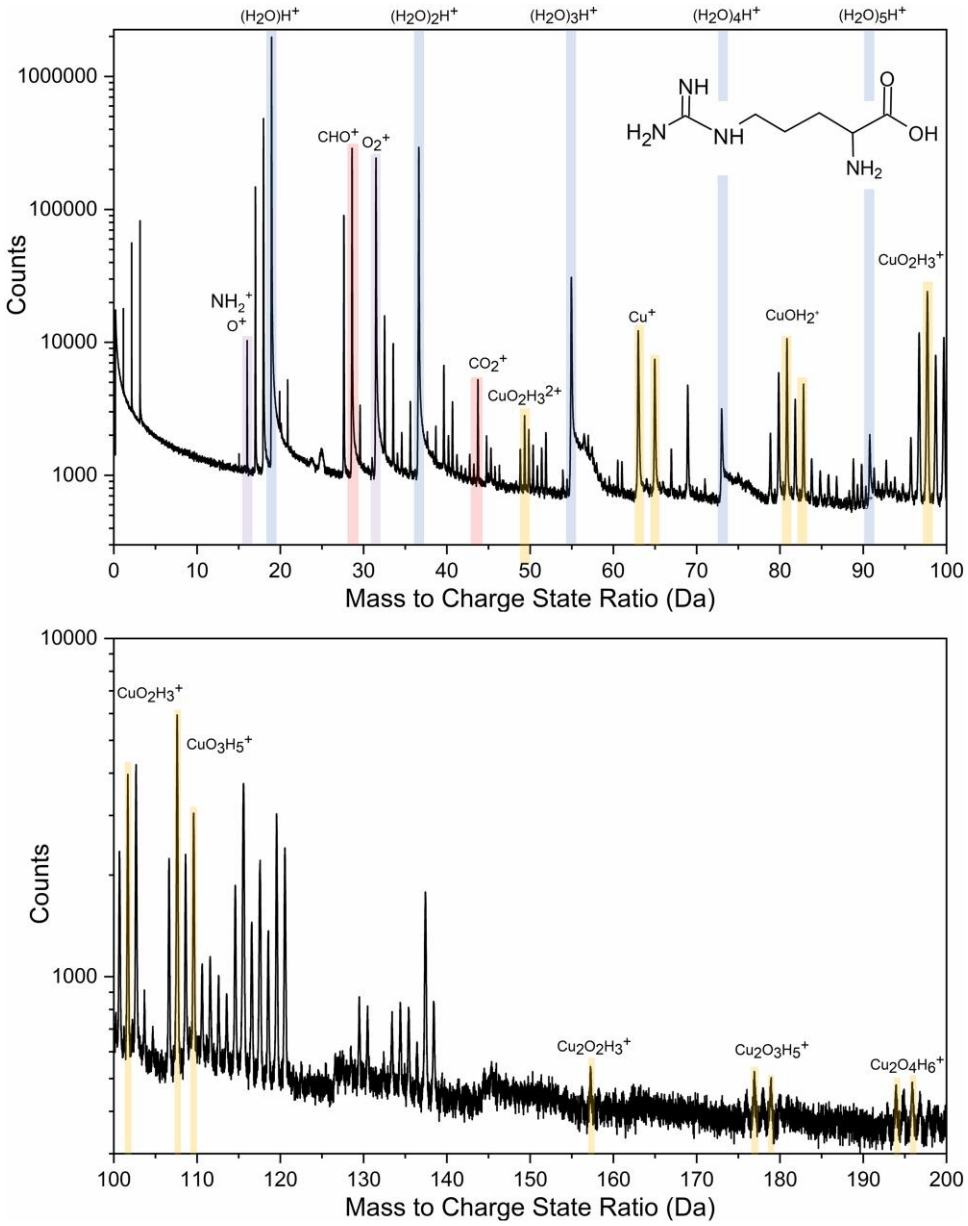

Fig. 3. Mass spectra subset for arginine on CuZn at 140 pJ LPE (35.6 million ions, CIR: 17.2, XS, Run 12, bin 0.1 Da). Both sections are plotted according to the magnitude of the largest peak, from 300 to 1 million counts on the top, and from 300 to 10,000 counts on the bottom. The vertical colored bars are added for visual emphasis only, where red is organic, blue is water clusters, purple represents ions which could be either one of two labeled possibilities or oxygen—one being an inorganic fragment, and dark yellow is copper.

heights exceeds 5.8% of the $^{63}Cu^+$ peak height as shown on the log plot. However, in other mass spectra, as discussed later, the height of those Cu oxide and water complexes can significantly exceed the $^{63}Cu^+$ peak height. The signal from Cu and their oxide species make it difficult to see any higher-ordered protonated water clusters above $n = 3$. Different from the other correlation histograms, Supplementary Figure S6 clearly shows ion tracks with a negative slope for both the 0–75 and 75–155 Da mass-to-charge regions, which correspond to the post-evaporation dissociations as discussed in the accompanying Supplementary Material, in which the endpoints are shown enlarged in Supplementary Figure S7. The peaks are not Ga^+ because the FIB used here uses monoisotopic ^{69}Ga; the ions converge to a 16 Da mass-to-charge line, indicating that that ion contains oxygen when it splits.

Arginine

A dataset containing over 140 million ions was acquired from a solution containing arginine, $C_6H_{14}N_4O_2$ with a mass of 174 Da, in Type 1 ultrapure DI water. A representative mass spectrum of the arginine solution is shown in Figure 3, with the chemical structure of the arginine inset at the upper right. The LPE was changed over the course of the analysis, with 40 M ions acquired at 40 pJ, then the energy was increased by 20 pJ every 5 million ions, until 140 pJ where 40 million ions were collected. Since no significant changes were seen, the data are not shown. As shown in Figure 3, protonated water cluster ions up to $n = 5$ are present when using 140 pJ LPE, along with a variety of signals stemming from the metallic substrate and organic fragments, with the most abundant

Downloaded from https://academic.oup.com/mam/article/31/4/ozaf032/8211905 by Forschungszentrum Juelich GmbH Zentralbibliothek user on 27 August 2025

labeled and identified. There are low-abundance higher mass clusters at mass-to-charge 173–180 and 193–199 Da respectively, which could be interpreted as either $Cu_2O_3H_x$ and $Cu_2O_4H_x$ or intact arginine and protonated arginine with one water of hydration. For clarification, organic compounds like carbohydrates or proteins have water molecules that are attached via hydrogen bonds to them. In the atom probe, these can field evaporate with over a dozen water molecules attached to carbohydrates, with repeated peaks separated by the mass of water. Such water molecules are defined as "waters of hydration" (Schwarz et al., 2021, 2022).

However, based on the results for the dataset in Supplementary Figure S8 showing the presence of Cu_2-cluster hydroxides at those mass-to-charge state ratios, they are more likely to be Cu_2^+-containing species. In order to try to identify changes in fragmentation of arginine or other ions caused by changes in the electrostatic field either caused by LPE changes or simply heterogeneous evaporation field of materials across the field-of-view (FoV), the data was segmented into two sections of 40 M ions acquired at 40 and 140 pJ LPE. In each of these two datasets, five cylindrical regions of interest (ROIs) were distributed in a grid pattern, and the calculated CIR for each ROI is shown in Supplementary Figure S9. A two-dimensional slice in the X–Y plane showing the CIR for the entire dataset is shown in Supplementary Figure S12.

These cylindrical ROIs in the two large sections of the dataset at different LPEs containing an amino acid provide an ideal environment to evaluate the influence of the CIR on the data. The datasets were each normalized internally to the highest peak abundance within that dataset, i.e., the $(H_2O)_1O^+$ peak. Figure 4a plots the water cluster abundance as a function of CIR, whereas Figure 4b shows the change in abundance versus CIR for various organic ions having mass-to-charge less than 60 Da, which can be attributed to organics. Above, there are too many interferences with Cu and Cu-containing ionic species to draw any conclusions. Finally, Figure 4c plots the mass spectra in the 10–55 Da region.

Three important observations can be concluded from these plots. First, the higher-order clusters $n = 2$–5 demonstrate the expected decline in abundance with increasing CIR, in contrast, the abundance of $(H_2O)_1H^+$ slightly increases with higher CIR. Similar CIRs have been observed for both voltage pulsing and laser pulsing (Woods et al., 2023*b*). The deviation in behavior for $(H_2O)_2H^+$ compared with the other clusters was previously noted (Anway, 1969; Stintz & Panitz, 1992, 1993; El-Zoka et al., 2020) and will require further investigations.

Second, the behavior of the organic fragments varies substantially when compared with the water clusters, in that water clusters largely decline with higher CIR and the organic ions are mostly relatively invariant on a log-scale plot. Note that the peak at mass-to-charge 16 Da may be O^+ or NH_2^+. The peak at mass-to-charge 34 Da is neither Cu-based nor water-based, and there is no sulfur in the solution or the considered amino acid. It is hence presumably organic in nature and could be $C_5H_8^{2+}$, i.e., corresponding to the complete C-backbone of the arginine. Even if rare, similar doubly charged carbonium ions have previously been reported (Beynon & Fontaine, 1966; Lammertsma et al., 1989; Vékey, 1995; Dass et al., 2005). Finally, as seen in Figure 4c, the level of background varies between datasets having different CIRs, which makes quantification challenging, since the peak heights will be different compared with the background. Since there was no effective way to remove the background consistently, it was not attempted. Overall, the evolution of the abundance appears to vary substantially by ion type and does not show as pronounced a trend as the protonated water signals/clusters.

Cysteine

Figure 5 plots the mass spectrum obtained from APT analysis of a solution of the sulfur-containing amino acid cysteine, $C_3H_7NO_2S$, with a mass of 121 Da, drop-cast onto NPG and plunge frozen, with the cysteine molecule inset in the upper right. The dataset is notable for the higher CIR of 73.2, where the very limited datasets collected at that CIR suggest that the abundance of H_2O^+ ions slightly increases compared with $(H_2O)_1H^+$, one possible explanation could be increased in the post-evaporation fragmentation of molecular ions, e.g., $(H_2O)_3H^+$ fragmenting into $(H_2O)_2H^+$ and H_2O^+ since at lower CIRs higher-order water clusters are observed. That probability would increase at higher electrostatic fields. A similar mechanism could also explain the higher fraction of lower-mass organic ions. The high amount of Au- and Ag-related ions in the spectrum, marked in gold and gray, respectively, can be seen as a result of the proximity to the substrate, which has been seen in previous work analyzing water in dealloyed NPG substrates (El-Zoka et al., 2020; Woods et al., 2024). There is a relatively large peak at mass-to-charge 35 Da, along with peaks at 32, 33, and 34, which could be related to S, which is unlikely, as discussed in the following paragraph.

To aid with the identification of S-containing peaks, pure S from a geological specimen was cryogenically prepared via liftout and coated with Cr (Schwarz et al., 2024). The corresponding mass spectrum is plotted in Supplementary Figure S10a. The two most abundant natural isotopes of S, i.e., greater than 1%, ^{32}S and ^{34}S, have relative abundances of 95.02 and 4.21%, respectively. In Supplementary Figure S10a,^{32} S^+ is dominant and visible above the background, but the $^{34}S^+$ peak cannot be visible, given that the peak height is less than 10-fold above the background; the notable mass-to-charge peak at 34 Da must therefore be SH_2^+ with secondary low-abundance SH^+ and SH_3^+ peaks as 33 and 35 Da, respectively. Next, mass spectra of arginine, a non-S-containing amino acid, show peaks at mass-to-charge 33 and 34 Da in the enlarged mass spectrum in Supplementary Figure S10b, therefore those peaks are organic and not S-derived.

There is a relatively large peak at mass-to-charge 35 Da in Figure 5. Since all amino acid solutions were prepared from hydrochloride salts, when comparing arginine and cysteine datasets as in Supplementary Figures S10b and S10c, respectively, a peak at mass-to-charge 35 Da is present in both. While Cl^+ or HCl^+ were not observed in the APT study of an aqueous solution containing NaCl (El-Zoka et al., 2020), those ions were observed in minerals and metals containing fluid inclusions (Dubosq et al., 2020, 2021) and in other specimens like sputtered (e.g., physical vapor deposition) films (El Azhari et al., 2019, 2022), corroded steel (Persdotter et al., 2021), and other geologic specimens (Darling et al., 2021). As discussed in the above references, the detection of Cl ions can be non-trivial. It was possible to detect Cl^+ in various systems (El Azhari et al., 2019; Dubosq et al., 2020, 2021; Persdotter et al., 2021), but it can also form Cl-containing cluster ions (El-Zoka et al., 2020).

Downloaded from https://academic.oup.com/mam/article/31/4/ozaf032/8211905 by Forschungszentrum Juelich GmbH Zentralbibliothek user on 27 August 2025

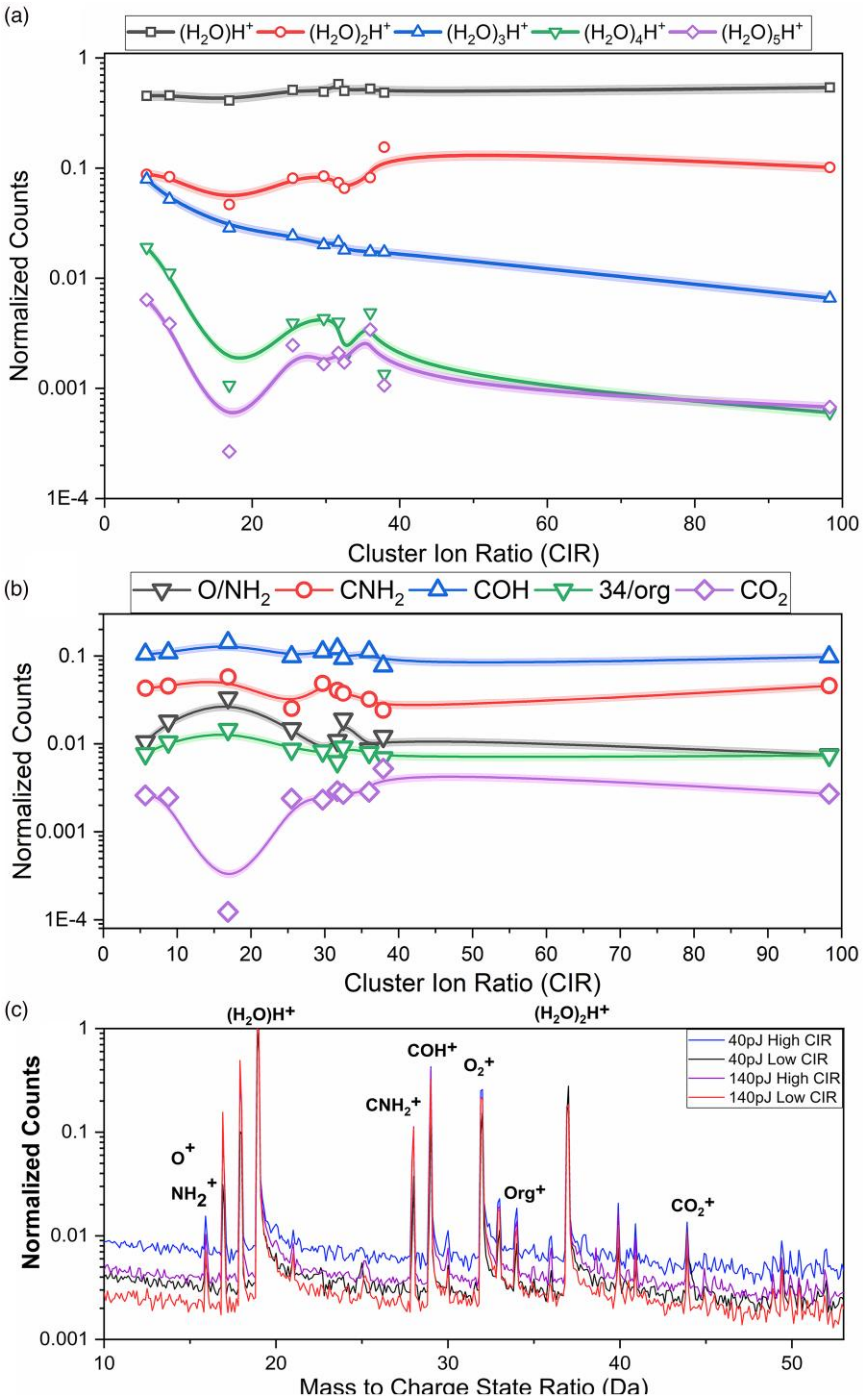

Fig. 4. Ion abundance derived from arginine dataset (XS, Run 12, Bin: 0.1 Da). (**a**) Protonated water cluster abundance plotted as a function of CIR. (**b**) The abundance of selected organic ions as a function of CIR, with a mass-to-charge state ratio less than 60 Da, and known Cu species in a double-charged ratio are excluded. (**c**) Mass spectrum for 15–55 Da region (Bin: 0.1 Da). The data were normalized to the maximum counts for the $(H_2O)_1H^+$ peak within each dataset so that they could be compared.

There are various reasons for this difficulty, for example, Cl and S overlap with many elements, as discussed above, and Cl specifically can form neutral species, e.g., Cl_2, during or after field evaporation. Since hydrochloride salts were used, the signal at 35 Da probably is Cl^+, but the $(H_2O)_2H^+$ peak at 37 Da is extremely high, meaning that the $^{37}Cl^+$ isotope cannot be used to check that. Although it is difficult to unambiguously define the peak at mass-to-charge 35 Da, it is assigned to Cl^+.

Discussion and Perspective

Substrate and Specimen Preparation

Metallic ions in solution are functionally impurities more likely found when the final tip of the specimen is in closer proximity to the metallic substrate. As discussed in Woods et al. (2023*a*), Exertier et al. (2024), and Tegg et al. (2024), Cu-containing molecular or cluster ions are commonly observed in APT of wet samples, whether created from chemically dealloyed CuMn, CuZn, or dissolved Cu incidental to

Downloaded from https://academic.oup.com/mam/article/31/4/ozaf032/8211905 by Forschungszentrum Juelich GmbH Zentralbibliothek user on 27 August 2025

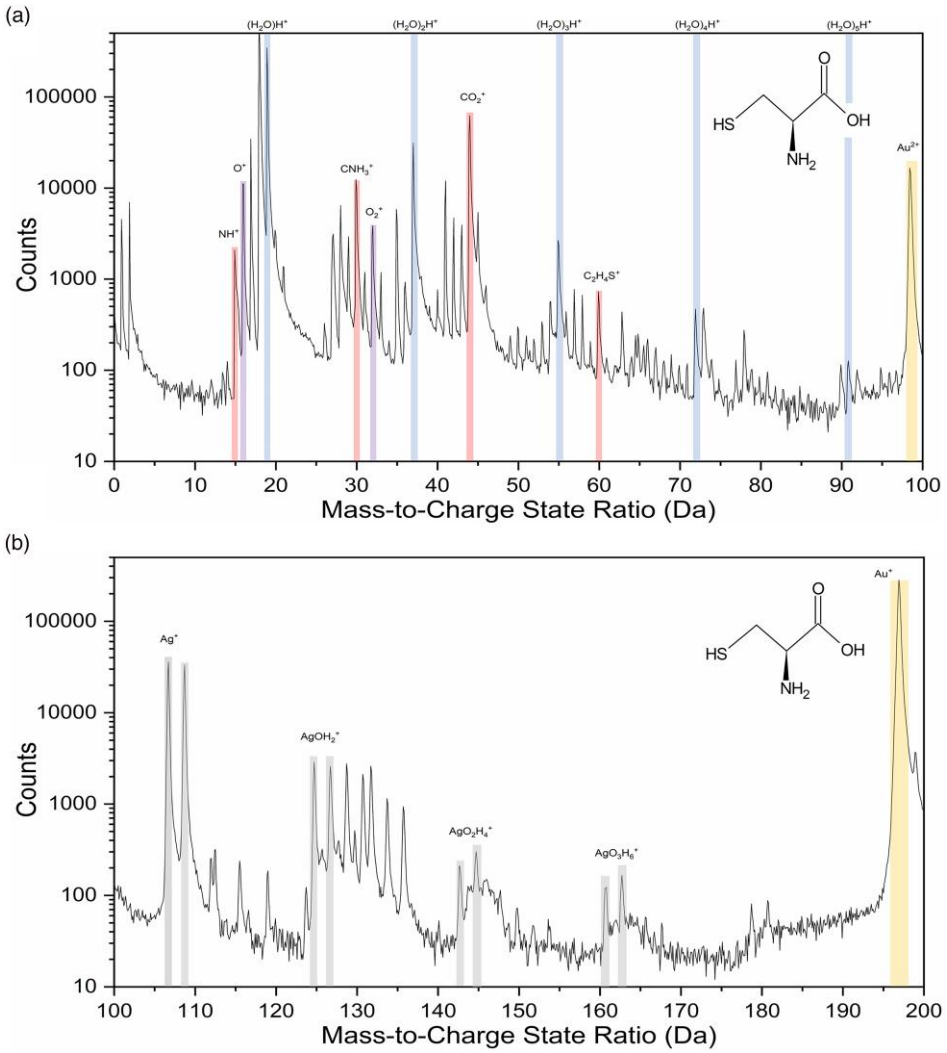

Fig. 5. Mass spectrum cysteine drop-cast onto NPG (4.5 million ions, CIR 73.2, XS, Run 9, Bin: 0.1 Da) (**a**) 0–100 Da and (**b**) 100–200 Da. The structure of cysteine is inset in the upper right. The mass spectrum is notable in that it does not contain peaks likely derived from S. If the sulfur moiety were present, it would be located at mass-to-charge 32 Da, although partially obscured by the O_2^+ ion contribution, and also at mass-to-charge 33 Da in the form of SH^+, possibly partially masked by the O_2^+ thermal tail. Note the occurrence of Ag–water clusters in (**b**). The colored lines are to visually emphasize particular labeled ions, here red is organic, blue is $(H_2O)_nH^+$, gray is Ag, purple is oxygen-based species, and darker yellow is Au.

graphene encapsulation. Likewise, Zn in the presence of O has been reported to evaporate in cluster form in the atom probe (Dawahre et al., 2011). In the context of organic compounds, free or solvated amino acids, particularly arginine and lysine, are known to form stable divalent metal (II) complexes with either copper or zinc (Bottari et al., 2014, 2019; Wu et al., 2022). This has been validated for most amino acids as well, although this does not seem to involve the terminal amine group for lysine (Smith et al., 1986; Conato et al., 2000) and likely not for arginine. At physiological pH or in water, all single, so-called free, amino acids are zwitterionic because the carboxyl and amine groups become ionized. Individual amino acids have different side groups, which can be charged. All amino acids are zwitterionic at neutral or physiological pH, but most are still electrically neutral at physiological pH. However, specific amino acids having charged side chains (e.g., lysine, arginine, and glutamate) and histidine are not electrically neutral in water, i.e., physiological pH, as discussed in Supplementary Material Section 1.3, with explanatory Supplementary Figures S11 and S12. However, assuming that amino acids are present in a protein and there is only one free carboxyl and amine group, respectively, on the ends of the peptide. Free amino acids in solution with both unterminated carboxyl and amine groups are therefore zwitterionic, and that would likely change the resulting evaporation and fragmentation compared with their dried form.

Separately, in the mass spectrum in Supplementary Figure S8, ions that likely correspond to $CuCN^+$ complexed with H_2O are found. These ions might form during the field evaporation process or with any amino acid in solution with a free amino group, and in any case can be related to the backbone amino group rather than the terminal ω-amine group in lysine or arginine's side chain (Conato et al., 2000).

The formation of such ions would definitely change the resultant mass spectrum and lead to the detection of those bonded amines as heavier molecular ions, but also change the relative abundances of other amino acid fragments. These higher-order fragments would substantially complicate the analysis and reconstruction of amino acids, because the spatial proximity of ions such as $Ag(CO)^+$, to other nitrogen-enriched fragments is

Downloaded from https://academic.oup.com/mam/article/31/4/ozaf032/8211905 by Forschungszentrum Juelich GmbH Zentralbibliothek user on 27 August 2025

necessary to determine the identity of specific molecules. Specifically, consider if an amine group bonded to a metal ion—that the amine group would not be obviously available to include an attempted reconstruction of a protein backbone. Additionally, for this work, the samples were manually plunged into a liquid nitrogen bath. The freezing rate was not sufficient to vitrify the samples, leading to the nonaqueous components of the solution segregating domain-like structures in the reconstructed APT data, particularly for the analysis of arginine in Supplementary Figure S9. These domains exhibit a higher CIR and a higher relative amount of multiple hits.

The further refinement and wider deployment of substrate-free FIB liftout techniques to prepare specimens from bulk frozen liquids are necessary to facilitate creating simpler mass spectra (Woods et al., 2023*b*), along with alleviating requirements for nanoporous metal substrates. Bulk sample preparation, through e.g., high-pressure freezing (HPF) that can create amorphous liquid discs over a hundred microns in thickness, will also help maintain the biomolecules in their native state. Such samples can then be transferred under cryogenic conditions in liquid nitrogen to the FIB and lifted out. This preparation method would avoid the need for nanoporous metals altogether. In the alternative or additionally, better preparation methods for nanoporous metals to completely remove the sacrificial metal (either Ag or Zn) would facilitate mass spectral analysis.

CIR and Electrostatic Field

The variations in specimen shape between experiments and during a single experiment can make it challenging to obtain reproducible data, and make the LPE a poor descriptor of the electrostatic field condition, as shown in Figure 1. The variation of the CIR across the FoV, as shown in Supplementary Figure S9, could partially have been expected based on the proximity to the location where the laser illuminates the specimen. The increased temperature there inherently has a lower electrostatic field and the tip shape becomes flatter on that side, as reflected in the lower CIR.

There are three levels of hierarchy and structure which are relevant here. At the microscale, as noted above, the tip shape is influenced by laser direction (Koelling et al., 2011). Since the slower freezing process results in incomplete vitrification of the liquid solution, organic-rich regions and domains are already visible in the SEM at a middle hierarchical level, e.g., on a scale of 20–30 nm based on current observations. These occur because the organic molecules can segregate into enriched domains at slower freezing rates. These domains are expected to have a higher evaporation field strength than water due to the covalent bonding within the molecules (Schwarz et al., 2022). These domains can create local topography through preferential evaporation of the surrounding water matrix (Miller, 1987; Vurpillot et al., 2000; Reddy et al., 2020; Schwarz et al., 2022). At an atomic or local level, the evaporation of the water matrix depends on cluster ion size (Schwarz et al., 2020). It has been shown that water clusters are pulled out of the surface of the tip and field evaporate (Segreto et al., 2022), which can lead to an inhomogeneous sample surface and thus to an uneven electrostatic field distribution. Therefore, some of the observed CIR variations are related to local composition variations because of the organic-rich regions found randomly within each sample cylinder, as well as to localized reshaping of the specimen under the combined influence of the laser pulsing and the intense electrostatic field (Schwarz et al., 2020).

The variations in specimen shape between experiments and during a single experiment can make it challenging to obtain reproducible data (Perea et al., 2008), and make the laser energy a poor descriptor to describe the electrostatic field conditions, as shown in Figure 1. As had been indicated in work on e.g., oxides (Schreiber et al., 2014; Singh et al., 2023) CSRs overall are a good electrostatic field strength proxy. The variation of the CIR across the FoV, as shown in Supplementary Figure S9, could partially have been expected based on the proximity to the location where the laser illuminates the specimen. The increased temperature in this region causes a specimen shape evolution to locally increase the curvature and leads to a lower electrostatic field on that specific side of the specimen (Sha et al., 2008), which is reflected by the lower CIR.

The overall implications of the CIR on the post-evaporation dissociation and fragmentation behavior of the individual molecular ions are yet to be quantified, but Figure 4b suggests a variability in both the fragmentation and abundance of those molecular ions. This introduces unnecessary variability and potential confounders into the data, including across the FoV. There are many unknowns as to whether the fragmentation depends on the molecule's orientation relative to the field evaporating surface (Wang et al., 2006), but it also likely depends on their local chemical environment, i.e., presence of spurious metals, that affect the local intensity of the electrostatic field. To some extent, this explains the APT data of proteinaceous structures, e.g., an IgG antibody embedded in a silica matrix (Sundell et al., 2019) showing extreme fragmentation, such that only CNH_3^+ and CO_2^+ ions were recovered in high proportion.

Fragmentation and Amino Acid Identification

Our data shows that it may be possible, even if challenging, to control the distribution of the collected fragments from amino acids, as shown in Figure 4. At lower CIR, one would generally expect heavier (larger) organic fragments to be detected, i.e., those ions less subject to fragmentation, but protonated water cluster ions up to higher orders will be measured, which can hinder the detection of heavier organic fragments. At higher CIR, lighter (smaller) fragments are detected, along with lower-order protonated water cluster ions, meaning that higher-order protonated water clusters are suppressed to the background along with increased fragmentation of larger molecular ions and less detection of those. Smaller fragments, on the one hand, would improve the spatial resolution, but a multiple of small fragments can lead to a more complex peak identification due to the high number of overlapping signals. On the other hand, the detection of larger fragments up to whole protonated molecules allows the localization and identification of whole organic molecules and their distribution in the 3D volume (Schwarz et al., 2021). There is hence a need to balance these two aspects in the optimization of the analysis conditions.

Practically, the identification of amino acids will likely be based on partial sets of fragments of the initial molecule. The lack of pronounced tracks or "hot spots" in the correlation histograms indicates that the field fragmentation takes place at the specimen's surface during the field evaporation process itself (Wang et al., 2006). It appears that the post-evaporation dissociation mechanism favors the removal of a

Downloaded from https://academic.oup.com/mam/article/31/4/ozaf032/8211905 by Forschungszentrum Juelich GmbH Zentralbibliothek user on 27 August 2025

hydroxyl group followed by the second oxygen (or the carboxylic acid group entirely), meaning that the identification of the amino acid will have to be based on molecular ions lacking oxygen. Those could also be complexed with metal ions which are in solution as well. These considerations have several implications for the identification of individual amino acids within proteins since practically the only difference in each amino acid is the side group. The identification of hydroxyl or carboxyl group will likely be one strategy for attempting to identify individual amino acids within a protein.

This work focused on three model amino acids in free form, where each has a carboxylic acid group on the one end (COOH). Since the other end has an amine group, the only oxygen atoms present are in the carboxyl group unless the side chain contains oxygen, which lysine, cysteine, and arginine do not. In the correlation histograms, no correlated evaporation of OH^+ (17 Da), H_2O^+ (18 Da), or CO_2^+ (44 Da) was observed, which means that the larger molecular ion that evaporates must lose a hydroxyl group, a carboxyl group, or both at the time they field evaporate. Since the available literature shows that when amino acids are analyzed in the atom probe (Nishikawa et al., 2000; Nishikawa & Taniguchi, 2017), COOH and OH are always observed, it logically follows that the hydroxyl/oxygen signal and carboxyl signal must come from the fragmentation of the end carboxyl group. As such, the remaining molecular ions would lack any remaining oxygen atoms. Some amino acids do have a side group that is terminated with a hydroxyl group, but most do not. Of the 20 canonical amino acids, 3 possess a hydroxyl group in the side chain (serine, threonine, and tyrosine), 2 contain a carboxyl group (aspartic acid and glutamic acid), and 2 contain amide groups ($CONH_2$). In the larger sense, when amino acids are linked into proteins, only one carboxyl group will exist at the terminal end of the protein. Any oxygen atoms would only be in the side chains, as in the study of dried amyloid fragments (Rusitzka et al., 2018) or in dipeptides (Taniguchi & Nishikawa, 2016; Nishikawa & Taniguchi, 2017).

One other significant factor for reconstructing water and biomolecules, which applies to oxides as well, is the consideration that both oxygen and nitrogen atoms tend to form neutral O_2 and N_2 species that are typically not detected, though their presence can be inferred from correlated evaporation histograms (Gault et al., 2016). Several pathways typically exist for oxygen to dissociate and form neutral species from oxides (Zanuttini et al., 2017). Likewise, the loss of nitrogen as neutrals has posed substantial problems in analyzing III–V nitrides in the atom probe (Morris et al., 2018, 2019; Zanuttini et al., 2018). However, it should be noted that in addition to possible non-detection of formed neutral species, there are several proposed mechanisms of loss here, as well as some other alternative explanations for the apparent ion loss. The extent to which neutral losses contribute to ion loss or non-detection here is still under active investigation.

Figure 6 plots the mass spectra for lysine in water on NPG, although with no visible metallic ions, versus cysteine in water on NPG with a CIR of 73.22. This CIR differential is substantial, although interestingly water clusters up to $n = 5$ appear visible in both cases. Overall, there are differences in the spectra, although the most common ion set for amino acids or proteins in the APT literature are still the most prominent, e.g., CO_2^+ and CNH_3^+/COH^+ (Nishikawa et al., 2011; Taniguchi et al., 2012; Taniguchi & Nishikawa, 2016; Sundell et al., 2019; Qiu et al., 2020*b*). Whether these differences are going to be exploitable to differentiate between amino acids will be the focus of future work. Yet, this result provides hope that amino acids can be differentiated by their side chain ionization patterns, which is encouraging for the future.

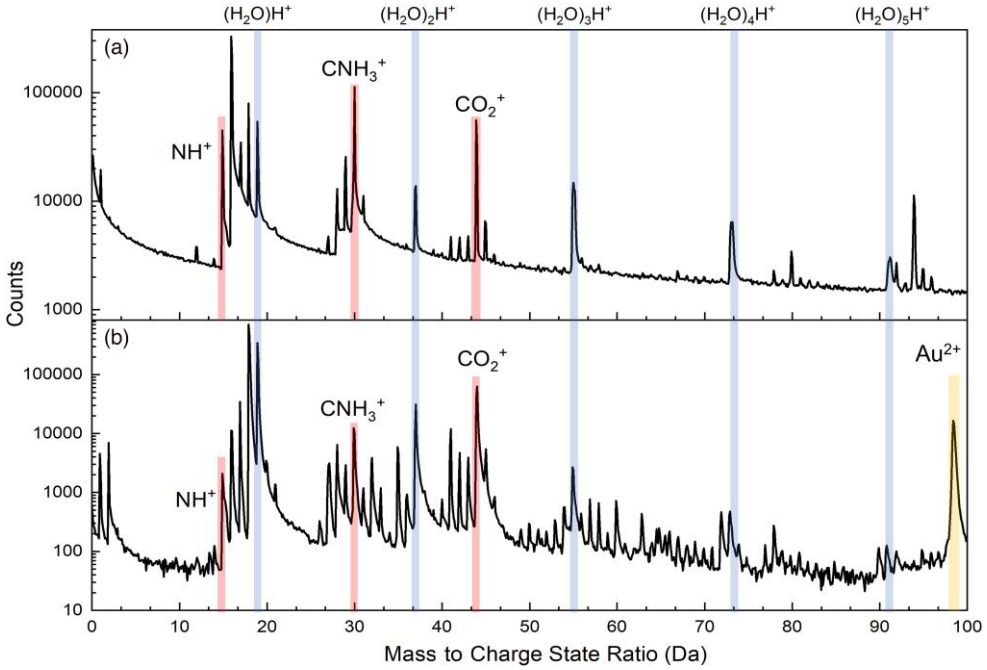

Fig. 6. Comparison of lysine dataset (CIR 3.82, XS, Run 8, Bin: 0.1 Da) versus cysteine (CIR 73.2, XS, Run 9, Bin: 0.1 Da) over same mass spectral range, limited range of 0–100 Da because of the metal ion overlaps starting at mass-to-charge 98.5 Da for Au^{2+}. Note that since COH^+ has the same mass as CNH_3^+, the ion is labeled as CNH_3^+ for visual simplicity. The vertical colored bars are added for optical emphasis only, where red is organic, blue is water clusters, gray is silver, and dark yellow is gold.

Downloaded from https://academic.oup.com/mam/article/31/4/ozaf032/8211905 by Forschungszentrum Juelich GmbH Zentralbibliothek user on 27 August 2025

Since amino acids are differentiated by their side chains, the close spatial proximity of certain fragments to each other and their mass is critical for the identification of amino acids from the otherwise identical protein backbone. For example, arginine has a characteristic, unique guanidinium group, $C(NH_2)_3^+$, on its side chain that ionizes at either 59 or 60 Da, depending on whether it is protonated or not. Lysine's side chain is terminated in an amino group, and overall has a mass of 71 Da if not ionized, so that side chain would be an important, distinct fragment.

The protein backbone is characterized by peptide bonds as N–C**α**–C–N–C**α**–C, where C is attached to oxygen with a double bond and thus helps create the unique character of the peptide bond. Since those are stronger than the single bonds of the side chain, the side chain would be predicted to ionize first. An expectation would be that, for example, some piece of the protein backbone would be ionized in proximity to a side group after it, so that the protein backbone could be reconstructed and the side group used to identify that particular amino acid, such as recent work by Sonal et al. (2023). The use of spatial clustering to identify the protein backbone in three dimensions, so as to facilitate computational reassembly and extraction of each amino acid, to form a protein sequence, requires machine learning because of the data volume and 3D spatial structure (Schmidt et al., 2018).

However, in order to firmly assign peak identities, *ab initio* and/or molecular dynamic simulations will be necessary, similar to e.g., Gu et al. (2020) but adjusted for the electrostatic field conditions in the atom probe (Zanuttini et al., 2017). As an example, the fragmentation behavior of glucose rings in a pure water solution under a high electrostatic field in the atom probe was facilitated by density functional theory simulations (Schwarz et al., 2021).

Perspectives on Future Work

APT is often considered to offer calibration-free quantitative analysis of materials. Although this may be (nearly) true for some metallic systems, this view likely needs to change, considering the field-dependence of the measurement accuracy and possible species-specific losses (Mancini et al., 2014; Gault et al., 2016; Zanuttini et al., 2017, 2018; Peng et al., 2019). To create fragmentation profiles for each amino acid, standardized reference spectra for each amino acid will likely need to be acquired beyond the cysteine and lysine presented here in this work. More specifically, the reference spectra should be acquired under similar local electrostatic fields, which the CIR can help guide and compare different datasets in the future with each other. This work demonstrates that the CIR affects peak heights in the mass spectra for two amino acids, at least via control of water clusters and controlling the overall background level. The fragmentation of lysine versus arginine as shown in Figures 2 and 3, as well as between lysine and cysteine in Figure 6, illustrates that there are substantial differences. These reference spectra can be used as spectral libraries, which can likely then be used to identify individual fragments and inform further amino acid identification, as has been done in MS for decades. The use of machine learning algorithms to predict the protein backbone position from spatial data, some of which already exist for cryo-TEM, can be used to facilitate that but will need dedicated adaptation for APT datasets (Si et al., 2020; Wei et al., 2021).

There is an elephant in the room, which is that electron imaging and Ga- or Xe-based FIBs used for preparing specimens have the potential to induce substantial damage (Warner et al., 2009; Peet et al., 2019; Daffner et al., 2020; Lucas & Grigorieff, 2023), including in metals (Gault et al., 2023; Saksena, 2024). For metallic materials, using cryogenic temperature during FIB-based APT specimen preparation has shown substantial benefits in damage reduction (Chang et al., 2019; Lilensten & Gault, 2020), however, for frozen liquids, little has been documented, and there are debates in the cryo-TEM community as to the extent and nature of electron- and different FIB-beam induced damage to TEM lamellas (Berger et al., 2023; Lucas & Grigorieff, 2023). Peaks pertaining to Xe or Ga are not typically observed in our analyses, but they may also be obscured by peaks pertaining to other molecular ions, and in metals, structural damage can extend tens of nanometers below where implanted ions are imaged (Saksena, 2024). The higher the observed metal concentration in a cryogenic water-based specimen, the more likely that, at least for Ga, there will be a Ga peak present. What part of the obtained results are affected by beam damage remains unknown, even if the expectation from previous work is that this will mostly affect the early stages of the APT analysis that are typically discarded from the analysis.

With regard to the complexity of the analyzed solution, a caveat is that for combinations of amino acids, the peptide bond will change the fragmentation and result in different spectra. Dipeptides, for example, lysine coupled with lysine, have been analyzed when dried on a small ball of CNT mesh using APT, where higher mass fragments corresponding to the combination peptide were observed (Taniguchi & Nishikawa, 2016; Nishikawa & Taniguchi, 2017). Those results demonstrate that higher mass molecular ions, which represent protonated dipeptides, can be detected, as well as dipeptide clusters combined with other fragments. Analysis of similar dipeptides in an aqueous solution should be tried to see whether comparable results can be achieved.

One could assume that the fragments from a single amino acid molecule will be detected in close proximity spatially and temporally—i.e., within a single pulse or over the next few pulses as had been shown previously for other material systems (De Geuser et al., 2007; Muller et al., 2011). However, when the large arginine dataset was thoroughly analyzed, higher-order multiple hits present in the filtered data (meaning three or more) look like the overall dataset, i.e., the evaporation is temporally uncorrelated. The need for high spatial resolution and high detection efficiency will likely favor the use of straight flight path atom probe systems, whereas most commercially available and active atom probe systems are reflectron-based, with approximately 50% ion loss, versus less than 20% for a straight flight path instrument. Then new targeted data processing tools for investigating spatial and temporal correlations between events, not unlike what has been used in the recent past to look for correlated events, will have to be developed (Katnagallu et al., 2019; Kim et al., 2024). There are additional benefits of using a straight flight path instrument beyond the detection efficiency, however.

To maximize the possibility of reconstructing and identifying biomacromolecules, the proportion of fragments from a single molecule that are detected must be maximized, in particular since the difference between individual amino acids in a peptide chain is limited to their side groups. In addition, in

Downloaded from https://academic.oup.com/mam/article/31/4/ozaf032/8211905 by Forschungszentrum Juelich GmbH Zentralbibliothek user on 27 August 2025

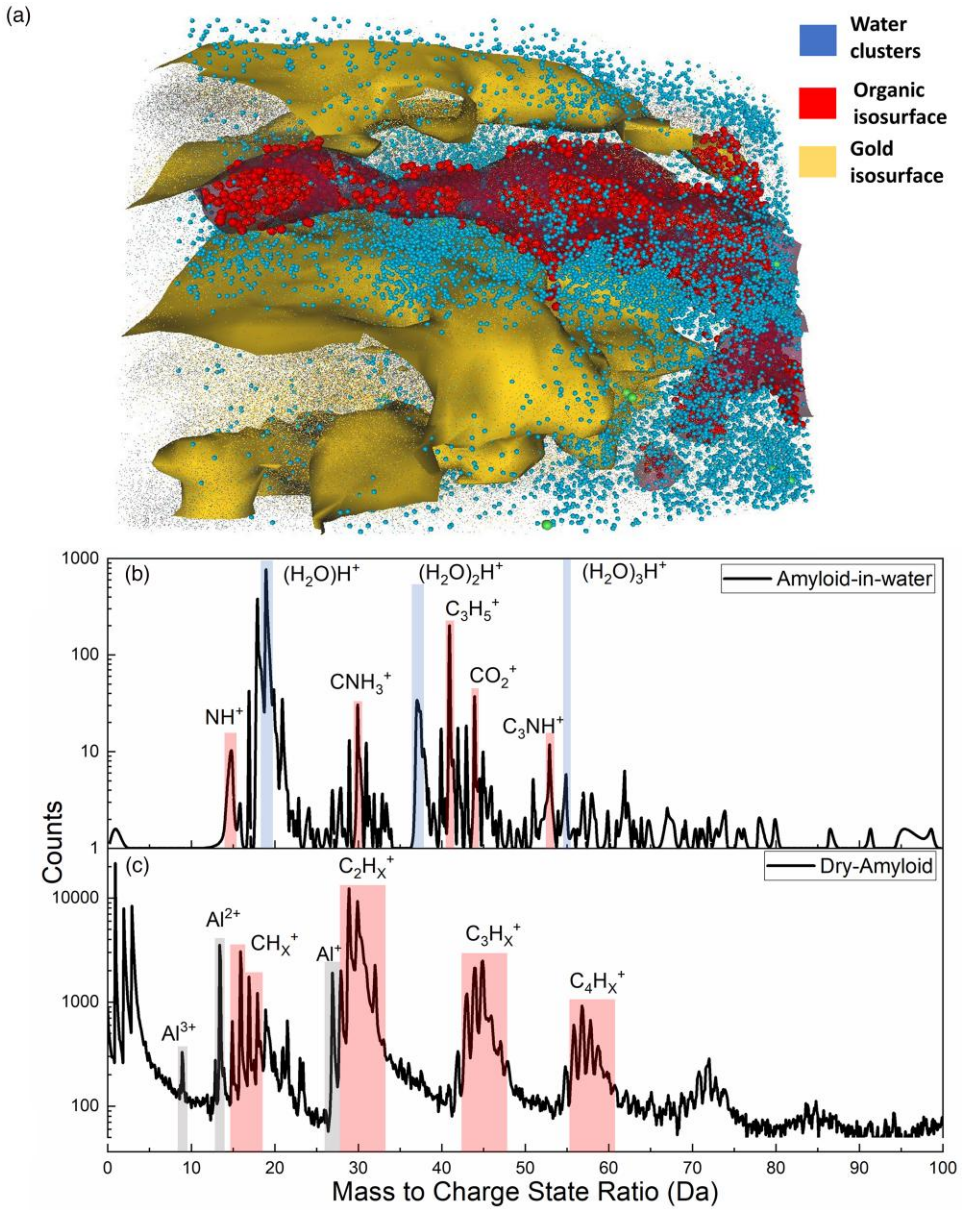

Fig. 7. (**a**) Visualization of an unlabeled amyloid Aβ1-42 fibril trapped in NPG pore [27 million ions (subset visualized), XS, Run 1, Bin: 0.1 Da], with protonated water clusters as blue spheres, and a gold isoconcentration surfaces that delineates regions containing over 70 at% (Au + Ag) and a red isodensity surface that encompasses regions containing C at or over 1.2% C at.nm-3. (**b**) Mass spectrum of hydrated organic material visualized in (**a**), e.g., an amyloid fibril, trapped in NPG pore, on limited mass range to 100 Da since Au^{2+} and other higher mass metal ions block visibility of any organic ions with higher mass [20k ions (subset)]. (**c**) Mass spectrum of original labeled Aβ1-42 amyloid fibrils dried on pre-sharpened Al tip with significant regions highlighted, taken from 31 (XS). The vertical colored bars are added for optical emphasis only, where red is organic, blue is water clusters, and gray is aluminum.

the future, to accurately reconstruct these molecules, the fragments must be filtered by close spatial proximity on the detector map, yet the fragments produced by molecular dissociations can lead to additional deflections (Blum et al., 2016; Peng et al., 2019), which result in different entry points into the reflectron with concomitant increase in "aberration" and are, in any case, harder to track than on a straight flight path instrument. There are also point density variations across the FoV in a reflectron-based system that make distance-based filtering more challenging to implement.

Ultimately, the goal is not to analyze individual amino acids but complex assemblies into proteins. Amyloid-beta monomers and oligomers, referred to as Aβ1-42, assemble in solution into the typical fibrils and plaques, first found in the brains of patients with Alzheimer's disease. In this case, the fibrils have a helical shape with an approximate diameter of 7 nm and varying length. One goal was to see if partially trapping such an amyloid fibril in a pore in the NPG to spatially confine it to a smaller analytical volume was possible. Here, we used unlabeled Aβ1-42 fibril in solution (Gremer et al., 2017), which were drop-cast and frozen by plunge freezing into LN2, transferred to the cryo-FIB for specimen preparation, and analyzed in the LEAP 5000 XS. An ROI inside the NPG containing is shown in Figure 7a, with protonated water cluster ions displayed as blue spheres, organic fragments in red, and the gold isoconcentration surface indicates the boundaries

Downloaded from https://academic.oup.com/mam/article/31/4/ozaf032/8211905 by Forschungszentrum Juelich GmbH Zentralbibliothek user on 27 August 2025

of the metallic pore. The red isoconcentration surface evidences a high carbon concentration consistent with a trapped amyloid fibril located inside an NPG pore. The mass spectrum for the data within the isoconcentration surface is plotted in Figure 7b. These fibrils were selected to allow for comparison with dried ^{13}C- and ^{15}N-labeled fibrils deposited onto an aluminum specimen as reported previously (Rusitzka et al., 2018). One of the mass spectra from these experiments is plotted in Figure 7c, and it consisted of hydrocarbon fragments, e.g., C_2H_x–C_4H_x in the dried form. These two mass spectra show a significantly different fragmentation pattern, which highlights the challenges lying ahead.

Finally, future work includes further development for sample preparation techniques, such as a combination of HPF vitrification and cryo-FIB/SEM preparation techniques for liftout from organic-containing bulk aqueous specimens to avoid the requirement for nanoporous metal substrates and the agglomeration of organic-rich regions; better chemical and thermal dealloying methods; development of standardized individual amino acid datasets; and machine learning methods for determining individual amino acid identities within individual proteins (Sonal et al., 2023).

Conclusion

To summarize, we have done a systematic study of model amino acids dissolved in pure water by APT. The CIR was introduced as an indicator of local electrostatic field conditions at the time of field evaporation for water-based samples, which appears repeatable across different atom probe systems, however the correlations between experimental conditions are neither direct nor straightforward as many parameters have an influence, to cite a few, the specimen's length, diameter, composition, the laser pulse energies and repetition rate, or the acquisition mode. Through analysis of lysine, arginine, and cysteine, we could demonstrate that different amino acids fragment in disparate patterns and, in principle, different side groups could be detected. Through analysis of the arginine dataset, we demonstrated that different CIR values produce different fragmentation ratios of lower-mass organic ions, which can be used in the future to tune the mass spectra. We then discussed the limitations of current approaches, particularly in terms of specimen preparation and analysis, along with the future development of optimized techniques for the identification of amino acid sequences within proteins and provide bounded guidance on which types of fragments are likely to be most consistently recoverable.

Availability of Data and Materials

The datasets used and/or analyzed during the current study available from the corresponding author upon request.

Supplementary Material

To view supplementary material for this article, please visit https://doi.org/10.1093/mam/ozaf032.

Acknowledgments

The authors would like to acknowledge Uwe Tezins for his assistance with the MPIE APT facility, and Andreas Sturm for his assistance in CAD design, probe fabrication, and FIB technique development. Additionally, the authors are grateful for the assistance of Jürgen Wichert in the MPIE metals workshop for vacuum dealloying techniques for copper and the MPIE mechanical workshop for their help in designing and manufacturing different sample holders, equipment holders, and other components with CNC and EDM, particularly Rainer Lück and Tristan Wickfeld. The advice of Dr James Douglas at Imperial College London for sample preparation and Dr. Shyam Katnagallu for data analysis is much appreciated, as is the initial help from Dr. Leigh Stephenson, now at the University of Sydney, while he was still at MPIE. Leonardo Shoji Aota is gratefully acknowledged for help and experimental support.

Financial Support

E.V.W., T.M.S., S.Z., I.M., and B.G. would like to acknowledge the DFG funding through the 2020 Leibniz Prize. B.G., I.M., A.E.Z., and S.H.K. would like to acknowledge funding through project SHINE (ERC-CoG) #771602 and the DFG through DIP Project No. 450800666. T.M.S. gratefully acknowledges the financial support of the Walter Benjamin Program of the German Research Foundation (DFG) (Project No. 551061178). D.W. was supported by "Portfolio Drug Research" of the "Impuls und Vernetzungs-Fonds der Helmholtzgemeinschaft".

Conflict of Interest

The authors declare that they have no competing interest.

References

Ajioka RS, Phillips JD & Kushner JP (2006). Biosynthesis of heme in mammals. *Biochim Biophys Acta* **1763**(7), 723–736. https://doi.org/10.1016/j.bbamcr.2006.05.005

Anway AR (1969). Field ionization of water. *J Chem Phys* **50**(5), 2012–2021. https://doi.org/10.1063/1.1671324

Balchin D, Hayer-Hartl M & Hartl FU (2020). Recent advances in understanding catalysis of protein folding by molecular chaperones. *FEBS Lett* **594**(17), 2770–2781. https://doi.org/10.1002/1873-3468.13844

Becker N, Frieg B, Gremer L, Kupreichyk T, Gardon L, Freiburg P, Neudecker P, Willbold D, Gohlke H & Heise H (2023). Atomic resolution insights into pH shift induced deprotonation events in LS-shaped Aβ(1-42) amyloid fibrils. *J Am Chem Soc* **145**(4), 2161–2169. https://doi.org/10.1021/jacs.2c09231

Berger C, Dumoux M, Glen T, Yee NB-Y, Mitchels JM, Patáková Z, Darrow MC, Naismith JH & Grange M (2023). Plasma FIB milling for the determination of structures in situ. *Nat Commun* **14**, 629. https://doi.org/10.1038/s41467-023-36372-9

Beynon JH & Fontaine AE (1966). Mass spectrometry: Inter-charge distance in doubly-charged organic ions. *Chemical Commun (London)* **20**, 717–719. https://doi.org/10.1039/C19660000717

Blavette D, Bostel A, Sarrau JM, Deconihout B & Menand A (1993). An atom probe for three-dimensional tomography. *Nature* **363**(6428), 432–435. https://doi.org/10.1038/363432a0

Blum I, Rigutti L, Vurpillot F, Vella A, Gaillard A & Deconihout B (2016). Dissociation dynamics of molecular ions in high DC electric field. *J Phys Chem A* **120**, 3654–3662. https://doi.org/10.1021/acs.jpca.6b01791

Bobalova J, Strouhalova D & Bobal P (2023). Common post-translational modifications (PTMs) of proteins: Analysis by up-to-date analytical techniques with an emphasis on barley. *J Agric Food Chem* **71**(41), 14825–14837. https://doi.org/10.1021/acs.jafc.3c00886

Bottari E, Festa MR & Gentile L (2014). Complex formation between zinc(II) and arginine in a large range of reagent concentration.

Downloaded from https://academic.oup.com/mam/article/31/4/ozaf032/8211905 by Forschungszentrum Juelich GmbH Zentralbibliothek user on 27 August 2025

Monatsh Chem Chem Mon **145**(11), 1707–1714. https://doi.org/10.1007/s00706-014-1279-5

Bottari E, Festa MR & Gentile L (2019). Complex formation between copper(II) and arginine in two ionic media and in a large range of reagent concentration. *Monatsh Chem Chem Mon* **150**(6), 1049–1058. https://doi.org/10.1007/s00706-019-02392-9

Bunton JH, Olson JD, Lenz DR & Kelly TF (2007). Advances in pulsed-laser atom probe: Instrument and specimen design for optimum performance. *Microsc Microanal* **13**(6), 418–427. https://doi.org/10.1017/S1431927607070869

Chang Y, Lu W, Guénolé J, Stephenson LT, Szczpaniak A, Kontis P, Ackerman AK, Dear FF, Mouton I, Zhong X, Zhang S, Dye D, Liebscher CH, Ponge D, Korte-Kerzel S, Raabe D & Gault B (2019). Ti and its alloys as examples of cryogenic focused ion beam milling of environmentally-sensitive materials. *Nat Commun* **10**, 942. https://doi.org/10.1038/s41467-019-08752-7

Chen L-L, Fan Y-G, Zhao L-X, Zhang Q & Wang Z-Y (2023). The metal ion hypothesis of Alzheimer's disease and the anti-neuroinflammatory effect of metal chelators. *Bioorg Chem* **131**, 106301. https://doi.org/10.1016/j.bioorg.2022.106301

Conato C, Contino A, Maccarrone G, Magrì A, Remelli M & Tabbì G (2000). Copper(II) complexes with L-lysine and L-ornithine: Is the side-chain involved in the coordination? *Thermochim Acta* **362**(1–2), 13–23. https://doi.org/10.1016/S0040-6031(00)00633-X

Cuduvally R, Morris RJH, Oosterbos G, Ferrari P, Fleischmann C, Forbes RG & Vandervorst W (2022). Post-field ionization of Si clusters in atom probe tomography: A joint theoretical and experimental study. *J Appl Phys* **132**(7), 074901-1–074901-13. https://doi.org/10.1063/5.0106692

Daffner K, Hanssen E, Norton I, Mills T, Ong L & Gras SL (2020). Imaging of dairy emulsions via a novel approach of transmission electron cryogenic microscopy using beam exposure. *Soft Matter* **16**, 7888–7892. https://doi.org/10.1039/D0SM00582G

Darling JR, White LF, Kizovski T, Černok A, Moser DE, Tait KT, Dunlop J, Langelier B, Douglas JO, Zhao X, Franchi IA & Anand M (2021). The shocking state of apatite and merrillite in shergottite Northwest Africa 5298 and extreme nanoscale chlorine isotope variability revealed by atom probe tomography. *Geochim Cosmochim Acta* **293**, 422–437. https://doi.org/10.1016/j.gca.2020.11.007

Dass C, Peake DA & Gross ML (2005). Structures of gas phase C5H8 radical cations: A collisional ionization study. *Org Mass Spectrom* **21**(11), 741–746. https://doi.org/10.1002/oms.1210211103

Dawahre N, Shen G, Balci S, Baughman W, Wilbert DS, Harris N, Butler L, Martens R, Kim SM & Kung P (2011). Atom probe tomography of zinc oxide nanowires. *J Electron Mater* **41**(5), 801–808. https://doi.org/10.1007/s11664-011-1803-x

De Geuser F, Gault B, Bostel A & Vurpillot F (2007). Correlated field evaporation as seen by atom probe tomography. *Surf Sci* **601**(2), 536–543. https://doi.org/10.1016/j.susc.2006.10.019

Devaraj A, Perea DE, Liu J, Gordon LM, Prosa TJ, Parikh P, Diercks DR, Meher S, Kolli RP, Meng YS & Thevuthasan S (2017). Three-dimensional nanoscale characterisation of materials by atom probe tomography. *Int Mater Rev* **63**(2), 68–101. https://doi.org/10.1080/09506608.2016.1270728

Di Russo E, Blum I, Rivalta I, Houard J, Da Costa G, Vurpillot F, Blavette D & Rigutti L (2020). Detecting dissociation dynamics of phosphorus molecular ions by atom probe tomography. *J Phys Chem A* **124**(52), 10977–10988. https://doi.org/10.1021/acs.jpca.0c09259

Douglas JO, Conroy M, Giuliani F & Gault B (2023). In situ sputtering from the micromanipulator to enable cryogenic preparation of specimens for atom probe tomography by focused-ion beam. *Microsc Microanal* **29**, 1009–1017. https://doi.org/10.1093/micmic/ozad020

Dubochet J, Adrian M, Chang J-J, Homo J-C, Lepault J, McDowall AW & Schultz P (1988). Cryo-electron microscopy of vitrified specimens. *Q Rev Biophys* **21**(2), 129–228. https://doi.org/10.1017/S0033583500004297

Dubosq R, Gault B, Hatzoglou C, Schweinar K, Vurpillot F, Rogowitz A, Rantitsch G & Schneider DA (2020). Analysis of nanoscale fluid inclusions in geomaterials by atom probe tomography: Experiments and numerical simulations. *Ultramicroscopy* **218**, 113092. https://doi.org/10.1016/j.ultramic.2020.113092

Dubosq R, Rogowitz A, Schneider DA, Schweinar K & Gault B (2021). Fluid inclusion induced hardening: Nanoscale evidence from naturally deformed pyrite. *Contrib Mineral Petrol* **176**(2), 15. https://doi.org/10.1007/s00410-021-01774-9

El-Zoka AA, Kim S-H, Deville S, Newman RC, Stephenson L T, Gault B (2020). Enabling near-atomic-scale analysis of frozen water. *Sci Adv* **6**, 6324. https://doi.org/10.1126/sciadv.abd6324

Elad N, Bellapadrona G, Houben L, Sagi I & Elbaum M (2017). Detection of isolated protein-bound metal ions by single-particle cryo-STEM. *Proc Natl Acad Sci U S A* **114**(42), 11139–11144. https://doi.org/10.1073/pnas.1708609114

El Azhari I, Barrirero J, García J, Soldera F, Llanes L & Mücklich F (2019). Atom probe tomography investigations on grain boundary segregation in polycrystalline Ti(C,N) and Zr(C,N) CVD coatings. *Scr Mater* **162**, 335–340. https://doi.org/10.1016/j.scriptamat.2018.11.041

El Azhari I, Barrirero J, Valle N, García J, von Fieandt L, Engstler M, Soldera F, Llanes L & Mücklich F (2022). Impact of temperature on chlorine contamination and segregation for Ti(C,N) CVD thin hard coating studied by nano-SIMS and atom probe tomography. *Scr Mater* **208**, 114321.

Exertier F, Tegg L, Taylor A, Cairney JM, Fu J & Marceau RKW (2024). Nanoscale analysis of frozen water by atom probe tomography using graphene encapsulation and cryo-workflows. *Microsc Microanal* **30**(6), 1181–1194. https://doi.org/10.1093/mam/ozae054

Forbes MW, Jockusch RA, Young AB & Harrison AG (2007). Fragmentation of protonated dipeptides containing arginine. Effect of activation method. *J Am Soc Mass Spectrom* **18**(11), 1959–1966. https://doi.org/10.1016/j.jasms.2007.08.003

Friedman M (1977). Mass spectra of cysteine derivates. *Adv Exp Med Biol* **86A**, 713–726. https://doi.org/10.1007/978-1-4684-3282-4_42

Gault B, Chiaramonti A, Cojocaru-Miredin O, Stender P, Dubosq R, Freysoldt C, Makineni SK, Li T, Moody M & Cairney JM (2021). Atom probe tomography. *Nat Rev Methods Primers* **1**(51), 1–51. https://doi.org/10.1038/s43586-021-00047-w

Gault B, Khanchandani H, Prithiv TS, Antonov S & Britton TB (2023). Transmission Kikuchi diffraction mapping induces structural damage in atom probe specimens. *Microsc Microanal* **29**(3), 1026–1036. https://doi.org/10.1093/micmic/ozad029

Gault B, Saxey DW, Ashton MW, Sinnott SB, Chiaramonti AN, Moody MP & Schreiber DK (2016). Behavior of molecules and molecular ions near a field emitter. *New J Phys* **18**, 33031. https://doi.org/10.1088/1367-2630/18/3/033031

Gault B, Vurpillot F, Vella A, Gilbert M, Menand A, Blavette D & Deconihout B (2006). Design of a femtosecond laser assisted tomographic atom probe. *Rev Sci Instrum* **77**(4), 043705-1–043705-8. https://doi.org/10.1063/1.2194089

Gerstl SSA & Wepf R (2015). Methods in creating, transferring, & measuring cryogenic samples for APT. *Microsc Microanal* **21**(S3), 517–518. https://doi.org/10.1017/S1431927615003384

Ghesquière P, Mineva T, Talbi D, Theulé P, Noble JA & Chiavassa T (2015). Diffusion of molecules in the bulk of a low density amorphous ice from molecular dynamics simulations. *Phys Chem Chem Phys* **17**, 11455–11468. https://doi.org/10.1039/C5CP00558B

Gordon LM & Joester D (2011). Nanoscale chemical tomography of buried organic-inorganic interfaces in the chiton tooth. *Nature* **469**, 194–197. https://doi.org/10.1038/nature09686

Grandfield K, Micheletti C, Deering J, Arcuri G, Tang T & Langelier B (2022). Atom probe tomography for biomaterials and biomineralization. *Acta Biomater* **148**, 44–60. https://doi.org/10.1016/j.actbio.2022.06.010

Gremer L, Scholzel D, Schenk C, Reinartz E, Labahn J, Ravelli RBG, Tusche M, Lopez-Iglesias C, Hoyer W, Heise H, Willbold D & Schroder GF (2017). Fibril structure of amyloid-β (1-42) by

Downloaded from https://academic.oup.com/mam/article/31/4/ozaf032/8211905 by Forschungszentrum Juelich GmbH Zentralbibliothek user on 27 August 2025

cryo-electron microscopy. *Science* **358**(6359), 116–119. https://doi.org/10.1126/science.aao2825
Gu M, Zhang J, Hase WL & Yang L (2020). Direct dynamics simulations of the thermal fragmentation of a protonated peptide containing arginine. *ACS Omega* **5**(3), 1463–1471. https://doi.org/10.1021/acsomega.9b03091
Halfon Y, Aspinall L, White J, Jackson Hirst I, Wang Y, Darrow MC, Muench SP & Thompson RF (2022). Maintaining the momentum in cryoEM for biological discovery. *Faraday Discuss* **240**, 18–32. https://doi.org/10.1039/D2FD00129B
Herdman M, von Kugelgen A, Kureisaite-Ciziene D, Duman R, El Omari K, Garman EF, Kjaer A, Kolokouris D, Lowe J, Wagner A, Stansfeld PJ & Bharat TAM (2022). High-resolution mapping of metal ions reveals principles of surface layer assembly in *Caulobacter crescentus* cells. *Structure* **30**(2), 215–228 e215. https://doi.org/10.1016/j.str.2021.10.012
Holmes NP, Roohani I, Entezari A, Guagliardo P, Mirkhalaf M, Lu Z, Chen Y-S, Yang L, Dunstan CR, Zreiqat H & Cairney JM (2023). Discovering an unknown territory using atom probe tomography: Elemental exchange at the bioceramic scaffold/bone tissue interface. *Acta Biomater* **162**, 199–210. https://doi.org/10.1016/j.actbio.2023.02.039
Houard J, Vella A, Vurpillot F & Deconihout B (2011). Three-dimensional thermal response of a metal subwavelength tip under femtosecond laser illumination. *Phys Rev B* **84**(3), 033405. https://doi.org/10.1103/PhysRevB.84.033405
Johnson PB & Christy RW (1972). Optical constants of the noble metals. *Phys Rev B* **6**(12), 4370–4379. https://doi.org/10.1103/PhysRevB.6.4370
Katnagallu S, Stephenson LT, Mouton I, Freysoldt C, Subramanyam APA, Jenke J, Ladines AN, Neumeier S, Hammerschmidt T, Drautz R, Neugebauer J, Vurpillot F, Raabe D & Gault B (2019). Imaging individual solute atoms at crystalline imperfections in metals. *New J Phys* **21**(12), 123020. https://doi.org/10.1088/1367-2630/ab5cc4
Kelly TF, Nishikawa O, Panitz JA & Prosa TJ (2009). Prospects for nanobiology with atom-probe tomography. *MRS Bull* **34**, 744–749. https://doi.org/10.1557/mrs2009.249
Kelly TF, Vella A, Bunton JH, Houard J, Silaeva EP, Bogdanowicz J & Vandervorst W (2014). Laser pulsing of field evaporation in atom probe tomography. *Curr Opin Solid State Mater Sci* **18**(2), 81–89. https://doi.org/10.1016/j.cossms.2013.11.001
Kessel A & Ben-Tal N (2018). *Introduction to Proteins: Structure, Function, and Motion*, 2nd ed. New York: Chapman and Hall/CRC.
Kim S-H, Bhatt S, Schreiber DK, Neugebauer J, Freysoldt C, Gault B & Katnagallu S (2024). Understanding atom probe's analytical performance for iron oxides using correlation histograms and ab initio calculations. *New J Phys* **26**(3), 033021. https://doi.org/10.1088/1367-2630/ad309e
Kingham DR (1982). The post-ionization of field evaporated ions: A theoretical explanation of multiple charge states. *Surf Sci* **116**(2), 273–301. https://doi.org/10.1016/0039-6028(82)90434-4
Klumpe S, Kuba J, Schioetz OH, Erdmann PS, Rigort A & Plitzko JM (2022). Recent advances in gas injection system-free cryo-FIB lift-out transfer for cryo-electron tomography of multicellular organisms and tissues. *Micros Today* **30**(1), 42–47. https://doi.org/10.1017/S1551929521001528
Koelling S, Innocenti N, Schulze A, Gilbert M, Kambham AK & Vandervorst W (2011). In-situ observation of non-hemispherical tip shape formation during laser-assisted atom probe tomography. *J Appl Phys* **109**(10), 104909-1–104909-6. https://doi.org/10.1063/1.3592339
La Fontaine A, Zavgorodniy A, Liu H, Zheng R, Swain M & Cairney J (2016). Atomic-scale compositional mapping reveals Mg-rich amorphous calcium phosphate in human dental enamel. *Sci Adv* **2**(9), e1601145. https://doi.org/10.1126/sciadv.1601145
Lammertsma K, Ragué Schleyer P & Schwarz H (1989). Organic dications: Gas phase experiments and theory in concert. *Angew Chem Int Ed Engl* **28**, 1321–1341. https://doi.org/10.1002/anie.198913211
Langelier B, Wang X & Grandfield K (2017). Atomic scale chemical tomography of human bone. *Sci Rep* **7**, 1–9. https://doi.org/10.1038/srep39958
Larson DJ, Prosa TJ, Ulfig RM, Geiser BP & Kelly TF (2013). *Local Electrode Atom Probe Tomography: A User's Guide*. New York: Springer Science + Business Media LLC.
Lee JM, Hammarén HM, Savitski MM & Baek SH (2023). Control of protein stability by post-translational modifications. *Nat Commun* **14**, 201. https://doi.org/10.1038/s41467-023-35795-8
Lee BEJ, Langelier B & Grandfield K (2021). Visualization of collagen-mineral arrangement using atom probe tomography. *Adv Biol (Weinh)* **5**(9), e2100657. https://doi.org/10.1002/adbi.202100657
Lilensten L & Gault B (2020). New approach for FIB-preparation of atom probe specimens for aluminum alloys. *PLoS One* **15**(4), e0231179. https://doi.org/10.1371/journal.pone.0231179
Lucas BA & Grigorieff N (2023). Quantification of gallium cryo-FIB milling damage in biological lamellae. *Proc Natl Acad Sci U S A* **120**(23), e2301852120. https://doi.org/10.1073/pnas.2301852120
Mancini L, Amirifar N, Shinde D, Blum I, Gilbert M, Vella A, Vurpillot F, Lefebvre W, Lardé R, Talbot E, Pareige P, Portier X, Ziani A, Davesnne C, Durand C, Eymery J, Butté R & Carlin J-F (2014). Composition of wide bandgap semiconductor materials and nanostructures measured by atom probe tomography and its dependence on the surface electric field. *J Phys Chem C* **118**, 24136–24151. https://doi.org/10.1021/jp5071264
Marsh JA & Teichmann SA (2015). Structure, dynamics, assembly, and evolution of protein complexes. *Annu Rev Biochem* **84**(1), 551–575. https://doi.org/10.1146/annurev-biochem-060614-034142
Miller MK (1987). The effects of local magnification and trajectory aberrations on atom probe analysis. *J Phys Colloques* **48**(C6), C6-565–C566-570. https://doi.org/10.1051/jphyscol:1987692
Morris RJH, Cuduvally R, Melkonyan D, Fleischmann C, Zhao M, Arnoldi L, van der Heide P & Vandervorst W (2018). Toward accurate composition analysis of GaN and AlGaN using atom probe tomography. *J Vacuum Sci Technol B* **36**(3), 03F130-1–03F130-6. https://doi.org/10.1116/1.5019693
Morris RJH, Cuduvally R, Melkonyan D, Zhao M, van der Heide P & Vandervorst W (2019). Atom probe of GaN/AlGaN heterostructures: The role of electric field, sample crystallography and laser excitation on quantification. *Ultramicroscopy* **206**, 112813. https://doi.org/10.1016/j.ultramic.2019.112813
Müller EW, Panitz JA & McLane SB (1968). The atom-probe field ion microscope. *Rev Sci Instrum* **39**(1), 83–86. https://doi.org/10.1063/1.1683116
Muller M, Saxey DW, Smith GDW & Gault B (2011). Some aspects of the field evaporation behaviour of GaSb. *Ultramicroscopy* **111**(6), 487–492. https://doi.org/10.1016/j.ultramic.2010.11.019
Nishikawa O, Ohtani Y, Maeda K, Watanabe M & Tanaka K (2000). Atom-by-atom analysis of diamond, graphite, and vitreous carbon by the scanning atom probe. *J Vacuum Sci Technol B Microelectron Nanometer Struct* **18**(2), 653–660. https://doi.org/10.1116/1.591256
Nishikawa O & Taniguchi M (2017). Toward the atomic-level mass analysis of biomolecules by the scanning atom probe. *Microsc Microanal* **23**, 336–339. https://doi.org/10.1017/S1431927616012551
Nishikawa O, Taniguchi M & Ikai A (2011). Atomic level analysis of amino acids by the scanning atom probe. *MRS Online Proc Libr* **1231**(3), 1–4. https://doi.org/10.1557/PROC-1231-NN06-09
Panitz JA (1982). Point-projection imaging of unstained ferritin clusters. *Ultramicroscopy* **7**(3), 241–248. https://doi.org/10.1016/0304-3991(82)90171-1
Panitz JA (2005). In search of the chimera: Molecular imaging in the atom-probe. *Microsc Microanal* **11**, 92–93. https://doi.org/10.1017/S1431927605500059
Peet MJ, Henderson R & Russo CJ (2019). The energy dependence of contrast and damage in electron cryomicroscopy of biological

Downloaded from https://academic.oup.com/mam/article/31/4/ozaf032/8211905 by Forschungszentrum Juelich GmbH Zentralbibliothek user on 27 August 2025

molecules. *Ultramicroscopy* **203**, 125–131. https://doi.org/10.1016/j.ultramic.2019.02.007

Peng Z, Zanuttini D, Gervais B, Jacquet E, Blum I, Choi P-P, Raabe D, Vurpillot F & Gault B (2019). Unraveling the metastability of C (n)(2+) (n = 2-4) clusters. *J Phys Chem Lett* **10**(3), 581–588. https://doi.org/10.1021/acs.jpclett.8b03449

Perea DE, Gerstl SSA, Chin J, Hirschi B & Evans JE (2017). An environmental transfer hub for multimodal atom probe tomography. *Adv Struct Chem Imaging* **3**(1), 12. https://doi.org/10.1186/s40679-017-0045-2

Perea DE, Wijaya E, Lensch-Falk JL, Hemesath ER & Lauhon LJ (2008). Tomographic analysis of dilute impurities in semiconductor nanostructures. *J Solid State Chem* **181**(7), 1642–1649. https://doi.org/10.1016/j.jssc.2008.06.007

Persdotter A, Boll T & Jonsson T (2021). Minor element effect on high temperature corrosion of a low-alloyed steel: Insight into alkali- and chlorine induced corrosion by means of atom probe tomography. *Corros Sci* **192**, 109779. https://doi.org/10.1016/j.corsci.2021.109779

Pinkerton TD, Scovell DL, Johnson AL, Xia B, Medvedev V & Stuve EM (1999). Electric field effects in ionization of water–ice layers on platinum. *Langmuir* **15**(3), 851–856. https://doi.org/10.1021/la980924o

Prosa TJ & Larson DJ (2017). Modern focused-ion-beam-based site-specific specimen preparation for atom probe tomography. *Microsc Microanal* **23**(2), 194–209. https://doi.org/10.1017/S1431927616012642

Qiu S, Garg V, Zhang S, Chen Y, Li J, Taylor A, Marceau RKW & Fu J (2020*a*). Graphene encapsulation enabled high-throughput atom probe tomography of liquid specimens. *Ultramicroscopy* **216**, 113036. https://doi.org/10.1016/j.ultramic.2020.113036

Qiu S, Zheng C, Garg V, Chen Y, Gervinskas G, Li J, Dunstone MA, Marceau RKW & Fu J (2020*b*). Three-dimensional chemical mapping of a single protein in the hydrated state with atom probe tomography. *Anal Chem* **92**(7), 5168–5177. https://doi.org/10.1021/acs.analchem.9b05668

Reddy SM, Saxey DW, Rickard WDA, Fougerouse D, Montalvo SD, Verberne R & Riessen A (2020). Atom probe tomography: Development and application to the geosciences. *Geostand Geoanal Res* **44**(1), 5–50. https://doi.org/10.1111/ggr.12313

Rusitzka KAK, Stephenson LT, Szczepaniak A, Gremer L, Raabe D, Willbold D & Gault B (2018). A near atomic-scale view at the composition of amyloid-beta fibrils by atom probe tomography. *Sci Rep* **8**, 17615. https://doi.org/10.1038/s41598-018-36110-y

Saksena A, Sun B, Dong X, Khanchandani H, Ponge D & Gault B (2024). Optimizing site-specific specimen preparation for atom probe tomography by using hydrogen for visualizing radiation-induced damage. *Int J Hydrog Energy* **50**, 165–174. https://doi.org/10.1016/j.ijhydene.2023.09.057

Saxey DW (2011). Correlated ion analysis and the interpretation of atom probe mass spectra. *Ultramicroscopy* **111**(6), 473–479. https://doi.org/10.1016/j.ultramic.2010.11.021

Schmidt JE, Peng L, Paioni AL, Ehren HL, Guo W, Mazumder B, Matthijs de Winter DA, Attila O, Fu D, Chowdhury AD, Houben K, Baldus M, Poplawsky JD & Weckhuysen BM (2018). Isolating clusters of light elements in molecular sieves with atom probe tomography. *J Am Chem Soc* **140**(29), 9154–9158. https://doi.org/10.1021/jacs.8b04494

Schreiber DK, Chiaramonti AN, Gordon LM & Kruska K (2014). Applicability of post-ionization theory to laser-assisted field evaporation of magnetite. *Appl Phys Lett* **105**(24), 244106-1–244106-5. https://doi.org/10.1063/1.4904802

Schreiber DK, Perea DE, Ryan JV, Evans JE & Vienna JD (2018). A method for site-specific and cryogenic specimen fabrication of liquid/solid interfaces for atom probe tomography. *Ultramicroscopy* **194**, 89–99. https://doi.org/10.1016/j.ultramic.2018.07.010

Schwarz TM, Dietrich CA, Ott J, Weikum EM, Lawitzki R, Solodenko H, Hadjixenophontos E, Gault B, Kastner J, Schmitz G & Stender P (2021). 3D sub-nanometer analysis of glucose in an aqueous solution by cryo-atom probe tomography. *Sci Rep* **11**(1), 11607. https://doi.org/10.1038/s41598-021-90862-8

Schwarz TM, Ott J, Solodenko H, Schmitz G & Stender P (2022). Nanoscale analysis of frozen honey by atom probe tomography. *Sci Rep* **12**(1), 17786. https://doi.org/10.1038/s41598-022-22717-9

Schwarz TM, Weikum EM, Meng K, Hadjixenophontos E, Dietrich CA, Kastner J, Stender P & Schmitz G (2020). Field evaporation and atom probe tomography of pure water tips. *Sci Rep* **10**(1), 20271. https://doi.org/10.1038/s41598-020-77130-x

Schwarz TM, Woods E, Singh MP, Chen X, Jung C, Aota LS, Jang K, Kramer M, Kim SH & McCarroll I (2024). In situ metallic coating of atom probe specimen for enhanced yield, performance, and increased field-of-view. *Microsc Microanal* **30**(6), 1109–1123. https://doi.org/10.1093/mam/ozae006

Segreto N, Schwarz TM, Dietrich CA, Stender P, Schuldt R, Schmitz G & Kastner J (2022). Understanding the underlying field evaporation mechanism of pure water tips in high electrical fields. *J Phys Chem A* **126**(33), 5663–5671. https://doi.org/10.1021/acs.jpca.2c04163

Sha G, Cerezo A & Smith GDW (2008). Field evaporation behavior during irradiation with picosecond laser pulses. *Appl Phys Lett* **92**(4), 043503-1–043503-3. https://doi.org/10.1063/1.2837626

Shuken SR (2023). An introduction to mass spectrometry-based proteomics. *J Proteome Res* **22**(7), 2151–2171. https://doi.org/10.1021/acs.jproteome.2c00838

Si D, Moritz SA, Pfab J, Hou J, Cao R, Wang L, Wu T & Cheng J (2020). Deep learning to predict protein backbone structure from high-resolution cryo-EM density maps. *Sci Rep* **10**(1), 4282. https://doi.org/10.1038/s41598-020-60598-y

Sigworth FJ (2016). Principles of cryo-EM single-particle image processing. *Microscopy (Oxf)* **65**(1), 57–67. https://doi.org/10.1093/jmicro/dfv370

Silaeva EP, Arnoldi L, Karahka ML, Deconihout B, Menand A, Kreuzer HJ & Vella A (2014). Do dielectric nanostructures turn metallic in high-electric dc fields? *Nano Lett* **14**(11), 6066–6072. https://doi.org/10.1021/nl502715s

Silaeva EP, Karahka M & Kreuzer HJ (2013). Atom probe tomography and field evaporation of insulators and semiconductors: Theoretical issues. *Curr Opin Solid State Mater Sci* **17**(5), 211–216. https://doi.org/10.1016/j.cossms.2013.08.001

Singh MP, Woods EV, Kim SH, Jung C, Aota LS & Gault B (2023). Facilitating the systematic nanoscale study of battery materials by atom probe tomography through in-situ metal coating. *Batter Supercaps* **7**(2), e202300403-1–e202300403-9. https://doi.org/10.1002/batt.202300403

Smith GG, Baum R & O'Brien P (1986). Further studies on the copper(II) complexes of lysine: $[Cu(II)(H_3N{\cdot}C_5H_{10}{\cdot}CH{\cdot}NH_2{\cdot}COO)_2]$ $[HgI_3]_2$. *Inorganica Chim Acta* **121**(1), 67–69. https://doi.org/10.1016/S0020-1693(00)87742-7

Sonal A, Wirth M, Doo Nam K, Moser T, Novikova I, Evans J & Perea D (2023). Towards resolving protein structures at the atomic scale using atom probe tomography. *Earth and Biological Sciences Directorate Conference*, Pacific Northwest National Laboratory (PNNL), Richland, Washington, February 23, 2023.

Stender P, Gault B, Schwarz TM, Woods EV, Kim S-H, Ott J, Stephenson LT, Schmitz G, Freysoldt C, Kastner J & El-Zoka AA (2022*a*). Status and direction of atom probe analysis of frozen liquids. *Microsc Microanal* **28**, 1150–1167. https://doi.org/10.1017/S1431927621013994

Stender P, Solodenko H, Weigel A, Balla I, Schwarz TM, Ott J, Roussell M, Joshi Y, Duran R, Al-Shakran M, Jacob T & Schmitz G (2022*b*). A modular atom probe concept: Design, operational aspects, and performance of an integrated APT-FIB/SEM solution. *Microsc Microanal* **28**, 1168–1180. https://doi.org/10.1017/S1431927621013982

Stephenson LT, Szczepaniak A, Mouton I, Rusitzka KAK, Breen AJ, Tezins U, Sturm A, Vogel D, Chang Y, Kontis P, Rosenthal A, Shepard JD, Maier U, Kelly TF, Raabe D & Gault B (2018). The Laplace Project: An integrated suite for preparing and transferring atom probe samples

Downloaded from https://academic.oup.com/mam/article/31/4/ozaf032/8211905 by Forschungszentrum Juelich GmbH Zentralbibliothek user on 27 August 2025

under cryogenic and UHV conditions. *PLoS One* **13**(12), e0209211. https://doi.org/10.1371/journal.pone.0209211

Stintz A & Panitz JA (1991). Imaging atom-probe analysis of an aqueous interface. *J Vacuum Sci Technol* **9**, 1365–1367. https://doi.org/10.1116/1.577628

Stintz A & Panitz JA (1992). Isothermal ramped field-desorption of water from metal surfaces. *J Appl Phys* **74**, 741–745. https://doi.org/10.1063/1.351860

Stintz A & Panitz JA (1993). Cluster ion formation in isothermal ramped field-desorption of amorphous water ice from metal surfaces. *Surf Sci* **296**(1), 75–86. https://doi.org/10.1016/0039-6028(93)90143-8

Stuve EM (2012). Ionization of water in interfacial electric fields: An electrochemical view. *Chem Phys Lett* **519–520**, 1–17. https://doi.org/10.1016/j.cplett.2011.09.040

Sundell G, Hulander M, Pihl A & Andersson M (2019). Atom probe tomography for 3D structural and chemical analysis of individual proteins. *Small* **15**(24), e1900316. https://doi.org/10.1002/smll.201900316

Taniguchi M & Nishikawa O (2016). Atomic level analysis of dipeptide biomolecules by a scanning atom probe. *J Vacuum Sci Technol B* **34**(3), 03H109-1–03H109-3. https://doi.org/10.1116/1.4941426

Taniguchi M & Nishikawa O (2019). Alternate field evaporation by changing laser pulsing and voltage pulsing dynamically for atom probe analysis. *Surf Interface Anal* **51**(1), 105–109. https://doi.org/10.1002/sia.6559

Taniguchi M, Nishikawa O & Ikai A (2012). Atomic level analysis of biomolecules by a scanning atom probe. *Surf Interface Anal* **44**(6), 721–723. https://doi.org/10.1002/sia.3873

Tegg L, McCarroll IE, Kim SH, Dubosq R, Woods EV, El-Zoka AA, Gault B & Cairney JM (2024). Analysis of water ice in nanoporous copper needles using cryo atom probe tomography. *Microsc Microanal* **30**(6), 1195–1204. https://doi.org/10.1093/mam/ozae062

Tegg L, McCarroll I, Sato T, Griffith M & Cairney J (2021). Nanoporous metal tips as frameworks for analysing frozen liquids with atom probe tomography. *Microsc Microanal* **27**(S1), 1512–1513. https://doi.org/10.1017/S1431927621005572

Vékey K (1995). Multiply charged ions. *Mass Spectrom Rev* **14**, 195–225. https://doi.org/10.1002/mas.1280140304

Vurpillot F, Bostel A & Blavette D (2000). Trajectory overlaps and local magnification in three-dimensional atom probe. *Appl Phys Lett* **76**(21), 3127–3129. https://doi.org/10.1063/1.126545

Vurpillot F, Gault B, Geiser BP & Larson DJ (2013). Reconstructing atom probe data: A review. *Ultramicroscopy* **132**, 19–30. https://doi.org/10.1016/j.ultramic.2013.03.010

Vurpillot F, Houard J, Vella A & Deconihout B (2009). Thermal response of a field emitter subjected to ultra-fast laser illumination. *J Phys D Appl Phys* **42**(12), 125502. https://doi.org/10.1088/0022-3727/42/12/125502

Wang LRC, Kreuzer HJ & Nishikawa O (2006). Polythiophene in strong electrostatic fields. *Org Electron* **7**(2), 99–106. https://doi.org/10.1016/j.orgel.2005.11.006

Warner JH, Schäffel F, Zhong G, Rümmeli MH, Büchner B, Robertson J & Briggs GAD (2009). Investigating the diameter-dependent stability of single-walled carbon nanotubes. *ACS Nano* **3**, 1557–1563. https://doi.org/10.1021/nn900362a

Warren SG (1984). Optical constants of ice from the ultraviolet to the microwave. *Appl Opt* **23**(8), 1206–1225. https://doi.org/10.1364/AO.23.001206

Wei Y, Varanasi RS, Schwarz T, Gomell L, Zhao H, Larson DJ, Sun B, Liu G, Chen H, Raabe D & Gault B (2021). Machine-learning-enhanced time-of-flight mass spectrometry analysis. *Patterns* **2**, 100192. https://doi.org/10.1016/j.patter.2020.100192

Woods EV, Kim S-H, El-Zoka AA, Stephenson LT & Gault B (2023a). Scalable substrate development for aqueous sample preparation for atom probe tomography. *J Microsc*, 1–14. https://doi.org/10.1111/jmi.13255

Woods EV, Saksena A, El-Zoka AA, Stephenson LT, Schwarz TM, Singh MP, Aota LS, Kim S-H, Schneider J & Gault B (2024). Nanoporous gold thin films as substrates to analyze liquids by cryo-atom probe tomography. *Microsc Microanal* **30**(6), 1172–1180. https://doi.org/10.1093/mam/ozae041

Woods EV, Singh MP, Kim S-H, Schwarz TM, Douglas JO, El-Zoka AA, Giulani F & Gault B (2023*b*). A versatile and reproducible cryo-sample preparation methodology for atom probe studies. *Microsc Microanal* **29**(6), 1992–2003. https://doi.org/10.1093/micmic/ozad120

Wu Z, Fu Z, Tian Y, Hasan M, Huang L, Yang Y, Li C, Zafar A & Shu X (2022). Fabrication and characterization of lysine hydrochloride Cu(II) complexes and their potential for bombing bacterial resistance. *Green Process Synth* **11**(1), 445–457. https://doi.org/10.1515/gps-2022-0043

Zanuttini D, Blum I, Rigutti L, Vurpillot F, Douady J, Jacquet E, Anglade P-M & Gervais B (2017). Simulation of field-induced molecular dissociation in atom-probe tomography: Identification of a neutral emission channel. *Phys Rev A (Coll Park)* **95**(6), 061401. https://doi.org/10.1103/PhysRevA.95.061401

Zanuttini D, Vurpillot F, Douady J, Jacquet E, Anglade P-M & Gervais B (2018). Dissociation of GaN(2+) and AlN(2+) in APT: Electronic structure and stability in strong DC field. *J Chem Phys* **149**(13), 134310. https://doi.org/10.1063/1.5036933

Zhang P, Chan W, Ang IL, Wei R, Lam MMT, Lei KMK & Poon TCW (2019). Revisiting fragmentation reactions of protonated α-amino acids by high-resolution electrospray ionization tandem mass spectrometry with collision-induced dissociation. *Sci Rep* **9**(1), 6453. https://doi.org/10.1038/s41598-019-42777-8

Zhang D, Wu L, Koch KJ & Cooks RG (1999). Arginine clusters generated by electrospray ionization and identified by tandem mass spectrometry. *Eur J Mass Spectrom* **5**(5), 353–361. https://doi.org/10.1255/ejms.295

Zhao L, Normand A, Houard J, Blum I, Delaroche F, Latry O, Ravelo B & Vurpillot F (2017). Optimizing atom probe analysis with synchronous laser pulsing and voltage pulsing. *Microsc Microanal* **23**, 221–226. https://doi.org/10.1017/S1431927616012666

Downloaded from https://academic.oup.com/mam/article/31/4/ozaf032/8211905 by Forschungszentrum Juelich GmbH Zentralbibliothek user on 27 August 2025